


2011

Two-Dimensional Computer Model of Human Atrial Ablation

Samineh R. Esfahani

University of South Florida, sesfahan@mail.usf.edu

Follow this and additional works at: <http://scholarcommons.usf.edu/etd>

 Part of the [American Studies Commons](#), and the [Biomedical Engineering and Bioengineering Commons](#)

Scholar Commons Citation

Esfahani, Samineh R., "Two-Dimensional Computer Model of Human Atrial Ablation" (2011). *Graduate Theses and Dissertations*. <http://scholarcommons.usf.edu/etd/3093>

This Thesis is brought to you for free and open access by the Graduate School at Scholar Commons. It has been accepted for inclusion in Graduate Theses and Dissertations by an authorized administrator of Scholar Commons. For more information, please contact scholarcommons@usf.edu.

Two-Dimensional Computer Model of Human Atrial Ablation

by

Samineh R. Esfahani

A thesis submitted in partial fulfillment
of the requirements for the degree of
Master of Science in Biomedical Engineering
Department of Chemical & Biomedical Engineering
College of Engineering
University of South Florida

Major Professor: Venkat Bhethanabotla, Ph.D.
Timothy J. Fawcett, Ph.D.
Robert Frisina Jr., Ph.D.

Date of Approval:
June 27, 2011

Keywords: Atrial Fibrillation, Cardiac Modeling, Atrial Electrograms, Ablation Model,
Excitation Propagation, AF Modeling, Finite Element Modeling, Bidomain Modeling,
Courtemanche Cell Model

Copyright © 2011, Samineh R. Esfahani

ACKNOWLEDGMENTS

I am extremely thankful to Dr. Venkat Bhethanabotla for the continuous support of my Master of Science research and study, for his encouragement, motivation, guidance, and immense knowledge. His generous support during my graduate study made my master study possible.

I owe my deepest gratitude to Dr. Timothy J. Fawcett for his immense guidance and support throughout the simulation process. He readily shared with me his vast knowledge and passion on the subject of MATLAB and COMSOL.

My sincere thanks also go to Dr. Raj Goyal whose guidance and support from the initial to the final level enabled me to develop an understanding of the subject of my studies.

Beside my advisors, I would like to thank Dr. Robert Frisina Jr. for agreeing to be on my thesis committee and reviewing my thesis.

In addition, I must also thank the Department, especially Karen Bray and Sandra Van Etten. They were always there to help, always there to guide. They are no longer with the department; however, I will always remember their genuine kindness.

Last but not the least, I would like to thank my family, and especially my parents, for their unconditional love and support throughout my life.

TABLE OF CONTENTS

LIST OF FIGURES	iii
ABSTRACT.....	vii
CHAPTER 1 INTRODUCTION	1
1.1 Problem Statement	1
1.2 Organization of the Thesis	3
CHAPTER 2 ATRIAL FIBRILLATION	5
2.1 Introduction	5
2.2 Prevalence and Incidence of Atrial Fibrillation	7
2.3 Normal Heart Electrical Activity vs. Atrial Fibrillation.....	8
2.4 Mechanism of Atrial Fibrillation.....	10
2.5 Atrial Fibrillation Treatment	10
2.6 The Limitations of the Catheter Ablation of Atrial Fibrillation.....	12
CHAPTER 3 ELECTRICAL ACTIVITY IN THE HEART.....	14
3.1 Introduction	14
3.2 Cardiac Action Potential	15
3.3 Measurement of Cardiac Electrical Activity (ECG)	18
3.4 Mathematical Modeling of Electrical Activity of the Heart.....	19
CHAPTER 4 ATRIAL TISSUE MODEL.....	21
4.1 Introduction	21
4.2 Courtemanche et al. Cell Model.....	22
4.2.1 Fast Na^+ Current	28
4.2.2 Time-Dependent K^+ Current.....	31
4.2.3 Transient Outward K^+ Current	31
4.2.4 Ultrarapid Delayed Rectifier K^+ Current	35
4.2.5 Rapid Delayed Rectifier K^+ Current	38
4.2.6 Slow Delayed Rectifier K^+ Current.....	40
4.2.7 L-Type Inward Ca^{2+} Current.....	41
4.2.8 Ca^{2+} Pump Current.....	44
4.2.9 Na^+ - K^+ Pump Current	45
4.2.10 Na^+ - Ca^{2+} Exchanger Current	46
4.2.11 Background Na^+ Current.....	47
4.2.12 Background Ca^{2+} Current	48

4.2.13 Ca^{2+} Uptake Current into NSR	48
4.2.14 Ca^{2+} Leak Current from NSR	49
4.2.15 Ca^{2+} Release Current from JSR	50
4.2.16 Ca^{2+} Transfer Current from NSR to JSR	52
4.2.17 Total Ionic Current.....	53
4.2.18 Atrial Cell Action Potential	54
4.3 Atrial Tissue Model.....	56
CHAPTER 5 ATRIAL ELECTROGRAM MODEL	61
5.1 Introduction	61
5.2 Electrogram Model.....	62
CHAPTER 6 ATRIAL FIBRILLATION ABLATION MODEL	68
6.1 Introduction	68
6.2 Complete Ablation	70
6.3 Fractional Ablation.....	71
6.4 The Effect of Change Conductivity.....	73
CHAPTER 7 CONCLUSIONS AND FUTURE WORK.....	75
7.1 Conclusions	75
7.2 Future Work	77
REFERENCES	78
APPENDICES	84
Appendix I Glossary	85
Appendix II Model Constants	88
Appendix III Copyright Permissions.....	90

LIST OF FIGURES

FIGURE 2 - 1 - Heart chambers and conduction system.....	5
FIGURE 2 - 2 - Average annual cost comparison between patient with and without AF.....	7
FIGURE 2 - 3 - Comparison of normal electrical activity of heart vs. atrial fibrillation.....	9
FIGURE 3 - 1 - Ventricular action potential.	17
FIGURE 3 - 2 - SA node action potential.....	18
FIGURE 3 - 3 - ECG waves and PR interval.....	19
FIGURE 4 - 1 - Schematic diagram of the cell model.....	23
FIGURE 4 - 2 - Ionic concentrations variable obtained with the Runge-Kutta (4,5) integration method.	25
FIGURE 4 - 3 - Steady state activation and inactivation curves of the fast Na^+ channel parameters.....	29
FIGURE 4 - 4 - Gating parameter variables of the fast Na^+ channel with the Runge-Kutta (4,5) integration method.....	30
FIGURE 4 - 5 - The fast Na^+ current in a period of 1000 ms and stimulus current at 100ms.....	30
FIGURE 4 - 6 - Time-dependent K^+ current in a period of 1000 ms and stimulus current at 100 ms.....	31
FIGURE 4 - 7 - Steady state activation and inactivation curves of the transient outward K^+ current parameters.....	33
FIGURE 4 - 8 - Gating parameter variables of the transient outward K^+ current at a period of 1000 ms.....	33

FIGURE 4 - 9 - Transient outward K ⁺ current in a period of 1000 ms and stimulus current at 100 ms.	34
FIGURE 4 - 10 - Steady state activation and inactivation curves of the ultrarapid delayed rectifier K ⁺ current parameters.	36
FIGURE 4 - 11 - Gating parameter variables of the ultrarapid delayed rectifier K ⁺ current at a period of 1000 ms.	36
FIGURE 4 - 12 - Ultrarapid delayed rectifier K ⁺ current in a period of 1000 ms and stimulus current at 100 ms.	37
FIGURE 4 - 13 - Steady state activation and inactivation curves of the rapid delayed rectifier K ⁺ current parameter.	38
FIGURE 4 - 14 - Gating parameter variables of the rapid delayed rectifier K ⁺ current at a period of 1000 ms.	39
FIGURE 4 - 15 - Rapid delayed rectifier K ⁺ current in a period of 1000 ms and stimulus current at 100 ms.	39
FIGURE 4 - 16 - Steady state activation and inactivation curves of the slow delayed rectifier K ⁺ current parameter.	40
FIGURE 4 - 17 - Gating parameter variables of the slow delayed rectifier K ⁺ current at a period of 1000 ms.	41
FIGURE 4 - 18 - Slow delayed rectifier K ⁺ current in a period of 1000 ms and stimulus current at 100 ms.	41
FIGURE 4 - 19 - Steady state activation and inactivation curves of the L-type inward Ca ²⁺ current parameters.	42
FIGURE 4 - 20 - Gating parameter variables of the L-type inward Ca ²⁺ current at a period of 1000 ms.	43
FIGURE 4 - 21 - L-type inward Ca ²⁺ current in a period of 1000 ms and stimulus current at 100 ms.	44
FIGURE 4 - 22 - Ca ²⁺ pump current in a period of 1000 ms and stimulus current at 100 ms.	45
FIGURE 4 - 23 - Na ⁺ - K ⁺ pump current in a period of 1000 ms and stimulus current at 100 ms.	46

FIGURE 4 - 24 - Na ⁺ - Ca ²⁺ exchanger current in a period of 1000 ms and stimulus current at 100 ms.....	47
FIGURE 4 - 25 - Background Na ⁺ current in a period of 1000 ms and stimulus current at 100 ms.	47
FIGURE 4 - 26 - Background Ca ²⁺ current in a period of 1000 ms and stimulus current at 100 ms.	48
FIGURE 4 - 27 - Ca ²⁺ uptake current into NSR current in a period of 1000 ms and stimulus current at 100 ms.....	49
FIGURE 4 - 28 - Ca ²⁺ leak current from NSR current in a period of 1000 ms and stimulus current at 100 ms.....	49
FIGURE 4 - 29 - Steady state activation and inactivation curves of the Ca ²⁺ release current from JSR parameters.....	51
FIGURE 4 - 30 - Gating parameter variables of the Ca ²⁺ release current from JSR at a period of 1000 ms.	51
FIGURE 4 - 31 - Ca ²⁺ release current from JSR current in a period of 1000 ms and stimulus current at 100 ms.....	52
FIGURE 4 - 32 - Ca ²⁺ current from NSR to JSR in a period of 1000 ms and stimulus current at 100 ms.....	52
FIGURE 4 - 33 - Total current in a period of 1000 ms and stimulus current at 100 ms.	53
FIGURE 4 - 34 - 12 ionic currents in a period of 1000 ms and stimulus current at 100 ms solved with the Runge-Kutta (4,5) integration method.	54
FIGURE 4 - 35 - Atrial cell membrane action potential.....	55
FIGURE 4 - 36 - Altered membrane action potential for a faster rate.	56
FIGURE 4 - 37 - Two-dimensional atrial tissue model.....	57
FIGURE 4 - 38 - Membrane action potential V as a function of time at 4 different locations.....	59
FIGURE 4 - 39 - Two-dimensional propagation of atrial action potential.....	60

FIGURE 5 - 1 - Two-dimensional atrial tissue with an electrode array and a stimulus region.....	62
FIGURE 5 - 2 - High right atrium electrogram obtained from a patient.	63
FIGURE 5 - 3 - Atrial electrograms were computed at 4 locations on unipolar electrodes..	64
FIGURE 5 - 4 - The background noise increases by increasing the electrode surface area by factors of 2 and 4..	65
FIGURE 5 - 5 - Unipolar electrogram computed in 4 different distances at the same location..	66
FIGURE 5 - 6 - Bipolar electrogram obtained from the difference between the electrograms recorded at two unipolar electrodes.	67
FIGURE 6 - 1 - Two-dimensional atrial tissue with a fractional ablation line.....	69
FIGURE 6 - 2 - Fibrillation induced to the model including a complete ablation line by rapid stimulation.....	70
FIGURE 6 - 3 - Two-dimensional propagation of action potential in a tissue with a complete ablation line.	71
FIGURE 6 - 4 - Fibrillation induced to the model including a fractional ablation line by rapid stimulation.....	72
FIGURE 6 - 5 - Two-dimensional propagation of action potential in a tissue with a fractional ablation line.....	73
FIGURE 6 - 6 - Atrial electrograms computed at the electrode 1 on tissue with a complete ablation line with electrical conductivities of 0.5, 0.1, 0.5, and 0 mS/m.	74

ABSTRACT

A finite-element model of a two-dimensional slice of human atrial tissue for the study of the electrograms and propagation of action potentials is presented. Action potential propagation is described by a reaction-diffusion model coupled with the complex Courtemanche et al. atrial cell model. The effects of recording electrode size and location on electrograms are presented. Action potential propagation as a result of atrial fibrillation ablation therapy is also modeled by defining a lesion area with decreased electrical conductivity. The effect of electrical conductivity and geometry of the lesion was also studied. It is shown that the success rate of atrial fibrillation ablation therapy is primarily correlated with the creation of continuous ablation lines and also the formation of fibrous tissue.

CHAPTER 1

INTRODUCTION

1.1 Problem Statement

Computational models of cardiac electrical activity and action potential propagation are becoming increasingly important for understanding the development and propagation mechanisms of arrhythmias and have received considerable attention recently. Atrial fibrillation (AF) is one of the most common arrhythmias, often leading to severe complications such as heart failure and stroke (Kannel et al, 1982).

Atrial fibrillation was first reported in 1909 as “*auricular fibrillation*”, common in people with heart disease (Lewis, 1909). Fibrillation means “to contract very fast and irregularly” (“What Is Atrial Fibrillation?”, 2009). AF occurs when disorganized electrical signals cause two upper chambers of the heart, atria, beat faster than rest of the heart. Therefore, the upper chambers of the heart cannot pump all the blood to the ventricles, the lower chambers of the heart causing the heart to not function normally. AF provokes discomfort and often leads to severe complications such as heart failure, blood clots, heart attack, and stroke. Heart failure complicated by AF is associated with excessive mortality (Stewart et al, 2002).

Radiofrequency ablation has emerged as a potential treatment for patients with AF with numerous studies over the past two decades aimed at improving the treatment

outcome. This technique involves positioning a catheter in the atrium and applying radiofrequency energy to the atrial tissue, causing changes in the electrical properties of the atrium thereby decreasing the future risk of fibrillation. The overall goals of this technique include removal of all potential triggers that may initiate fibrillation and to alter the conduction properties of the atria such that fibrillation cannot be sustained even when triggered.

One of the most common approaches to this modification is to create continuous transmural linear lesions that form barriers to conduction. (Earley & Schilling, 2006) The main goal of creating ablation lines in the atria is to create insulated barriers in the tissue to redirect the disorganized signals to follow a normal pathway. It is very important to create a continuous and transmural ablation lines. Any discontinuities in the ablation line can lead to the reentries and sustaining the fibrillation (Thomas, 1999).

Creating linear lesions in the tissue destroys some excitable cells and alters the conductivity properties of the tissue. Ablated areas are replaced by fibrous tissues during healing (Haines, 2000) with an electrical conductivity lower than normal tissue and thereby altering the conduction properties.

The use of computers and numerical models to reproduce heart electrograms and action potential is not recent. There are numerous designs in simulating the electrical propagation in the heart tissue. Generally, these models are extremely demanding in terms of computational resources.

Less computationally demanding model is based on less detailed atrial cell models such as the Fitz-Hugh-Nagumo model with 1 or 2 variables which is far less

accurate than the more complex ion-channel models such as Courtemanche et al. model with 21 variables (Courtemanche et al. 1998) (Fitz-Hugh, 1961).

This work presents a detailed numerical study of a two-dimensional slice of human atrial tissue using the complex Courtemanche et al. atrial cell model.

There are several advantages in reproducing arrhythmias in a numerical model compared to the vivo experiments:

- Having a full control of all parameters in the model.
- Predicting the experiment results
- Reproducing the experiments and results
- Having a full access to data compared to a few parameters in vivo experiments.

The ultimate goal of this thesis is:

- To develop a realistic numerical model of atrial electrograms recorded via a mapping catheter.
- To better understand the action potential propagation as a result of atrial fibrillation ablation therapy.

1.2 Organization of the Thesis

This thesis is organized in six chapters.

Chapter 2 presents a brief overview of the overall function of the human cardiovascular system and atrial fibrillation. The prevalence and incidence of atrial fibrillation are presented. It also discusses the currently available ablation procedure for atrial fibrillation treatment.

Chapter 3 presents an overview in the electrical activity in the heart and the concepts of cell excitability and action potential. A description of the principal ions involved in the action potential is provided. The basics of myocardial action potential and electrocardiogram (ECG) are introduced in conjunction with the standard mathematical model of cardiac action potential.

Chapter 4 describes a mathematical cell model of atrial human myocyte by Courtemanche et al. The model is regenerated and solved with a various integration methods. The comparison of the model solved with two different methods is presented. The mathematical atrial tissue model is also presented as well as atrial action potential propagation in a two-dimensional model.

Chapter 5 discusses the mathematical model of atrial electrograms. It presents the unipolar and bipolar electrogram models. The results are compared to the human data. It describes the effect of the catheter electrode characteristics on the shape of the atrial electrogram signals.

Chapter 6 presents the atrial fibrillation ablation model. Atrial fibrillation is induced to the model. Then, the effects of the complete ablation and fractional ablation on propagation of atrial fibrillation are shown. It also discusses the effect of electrical conductivity of the ablation line on the propagation of action potential in a two-dimensional tissue.

Chapter 7 concludes the thesis with a discussion of the main developments of this thesis and possible future works.

CHAPTER 2

ATRIAL FIBRILLATION

2.1 Introduction

Heart disease is the leading cause of death worldwide with approximately, 700,000 deaths every year (Minino et al. 2007). The heart made of four chambers: right atrium, left atrium, right ventricle and left ventricle pumps blood throughout the body to supply oxygen and nutrients for other organs (FIGURE 2 - 1).

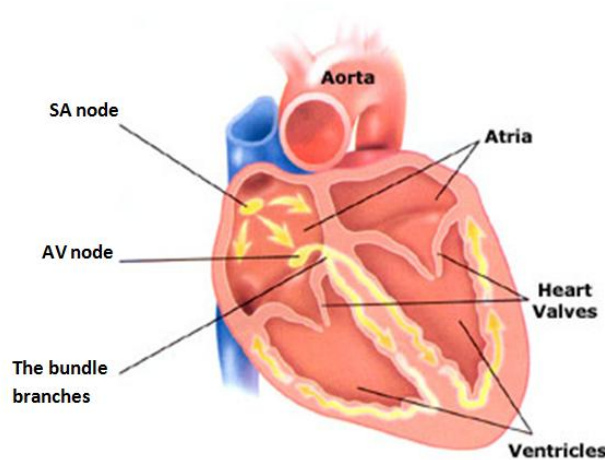


FIGURE 2 - 1 - Heart chambers and conduction system. (Tyler Cardiovascular Consultants, 2008)

The right side of the heart receives and pumps blood low in oxygen and the left side of the heart receives and pumps blood high in oxygen. The mechanical activity of the heart is controlled by the electrical activity in the heart. Conduction system of the heart

consists of the sinoatrial node (SA), interatrial pathway, atrioventricular node (AV), intermodal pathway, atrioventricular bundle (AV bundle and bundle of His), right and left bundle branches, and Purkinje fibers.

The rhythmic or pacing signal is normally generated at the SA node and spreads throughout the left and right atrium causing them to contract and pump blood into the ventricles through the open valves. Then the signal reaches the AV node and quickly spreads throughout the left and right ventricular causing them to contract and pump the blood out of the heart. As the ventricles begin to contract, the atria have completed their contraction. The atria relax until the arrival of next impulse from, the SA node. This process occurs during the normal heart beat. The SA node is able to generate between 50 and 150 impulses per minute depending on body requirements. Heart electrical activities can be recorded via electrodes placed on the chest. The graphical picture of the heart electrical signals is called an electrocardiogram (ECG or EKG).

Abnormal electrical activity in the heart known as heart arrhythmia, cause the heart to beat too slow, too fast or irregular. Most arrhythmias are risk-free, but some can be very serious or even life threatening and result in sudden death (Benjamin, 1994).

Atrial Fibrillation is one of the most common arrhythmias that often lead to severe complications such as heart failure and stroke. AF is associated with excess mortality and is a growing problem that needs attention.

2.2 Prevalence and Incidence of Atrial Fibrillation

Atrial arrhythmias are clinically important because they are so common. Atrial fibrillation alone occurs in 0.95 % of the general population. AF is more common in men than women and its prevalence increases with age, ranging from 0.1% in persons below 55 years and 9.0% in persons above 80 years (Go, et al., 2001) .

AF affects more than 2 million Americans, and its prevalence is projected to increase to more than 5.6 million by the year 2050 as a result of the aging population (Go, et al., 2001).

Medical costs for patients with AF have been found to be 5-fold higher than those without the disease (Wu, et al., 2005). AF treatment cost is estimated at \$6.65 billion in the U.S. in 2005 (Andrikopoulos et al. 2009). Breaking out this total into the categories of drugs and hospital inpatient, outpatient, and other costs (eg. laboratory), patients with AF have higher costs than non-AF patients in each category (FIGURE 2 - 2) (Wu, et al., 2005).

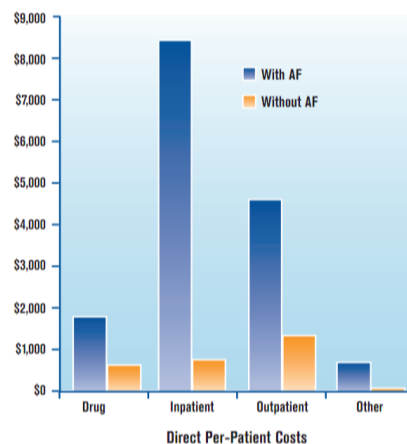


FIGURE 2 - 2 - Average annual cost comparison between patient with and without AF. (Wu, et al., 2005)

The number of patients with atrial fibrillation is increasing significantly. Therefore coordinated efforts are needed to optimize the treatment methods of atrial fibrillation to substantially increase the success rate and reduce the cost of hospitalization and medication.

2.3 Normal Heart Electrical Activity vs. Atrial Fibrillation

In AF, the heart electrical signals begin in several areas of the atrial wall, mainly in nearby pulmonary veins instead of the SA node. These signals usually spread throughout the atria in a rapid, disorganized way as they do not follow a normal pathway, causing the atria to fibrillate. This also affects the ventricles and makes them to beat very fast. However, the ventricles still cannot beat as fast as the atria. Thus, the ventricles and atria do not beat in the same rate and it causes heart arrhythmia. In AF, the ventricles beats at the rate of 100 to 175 beats per minute when the normal rate is 60 to 100 beats per minute ("What Is Atrial Fibrillation?", 2009).

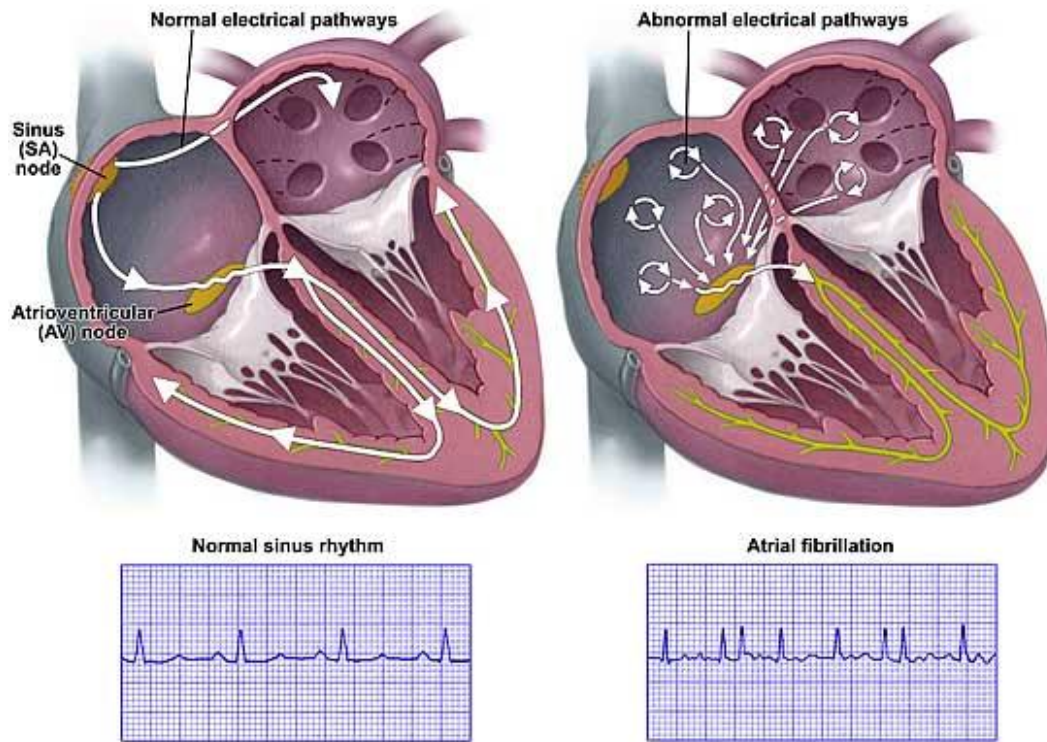


FIGURE 2 - 3 - Comparison of normal electrical activity of heart vs. atrial fibrillation. The left figure shows the normal electrical pathways in the heart. The right figure shows the abnormal electrical pathways that occur during Atrial Fibrillation. (Fowler, 2010)

There are different types of AF: paroxysmal, persistent, and permanent ("What Is Atrial Fibrillation?", 2009). In paroxysmal AF, the abnormal heart rhythm begins suddenly and stops on its own and usually last between 24 hours to 7 days. People with paroxysmal AF usually have episodes unexpectedly every day or only a few times a year, and can be dangerous (Schoenstadt, 2006). Persistent AF lasts more than 7 days and does not self-terminate. With treatment required to stop the abnormal rhythm. In permanent AF, the abnormal rhythm cannot be treated and the normal heart rate cannot be restored ("What Is Atrial Fibrillation?", 2009).

2.4 Mechanism of Atrial Fibrillation

There are two hypotheses of atrial fibrillation: the multiple wavelet and the focal source hypotheses (Rosenthal, 2010). The multiple wavelet hypothesis states that AF “would be generated by various wavefronts that would spread throughout the excitable atrial tissue” (Fernández, 2006). The focal source hypothesis proposes that AF would be initiated and maintained by some high frequency sources in some regions of the atrial tissue, especially nearby pulmonary veins (Fernández, 2006).

Which mechanism precisely causes AF is not completely understood. According to observations over the last decade, both hypotheses are important in the mechanism of AF (Rosenthal, 2010). Research indicates the importance of focal triggers, particularly triggers of the pulmonary veins in the formation of reentrant wavefronts generated by irregular propagation of electrical signals (Khairy & Nattel, 2002).

Atrial Fibrillation can be diagnosed during an electrocardiogram (ECG) recording. AF is distinguished from a normal rhythm with the presence of irregular function in the baseline of the ECG (Lead III and VI), absence of the P wave which illustrates atrial contraction as well as irregular R-R interval time duration between two R waves of the ECG (Patel et al. 2000).

2.5 Atrial Fibrillation Treatment

Atrial fibrillation can be treated by several methods including various medications, nonsurgical procedures, pacemakers, and/or surgical procedures. The goal

of all these treatments is to restore normal heart rhythm (Falk & Podrid, 1997). Studies show that the long-term antiarrhythmic medication for the treatment of AF is associated with a high rate failure (Stewart et al. 2002). Moreover, antiarrhythmic agents are focused more on the ventricular rate control not the atrial activity. Therefore, the most common treatment option available today is catheter ablation. In catheter ablation, some regions of the atrium tissue are burnt using a source of energy, usually radiofrequency pulses cause extensive tissue damage at the ablation site. As a result, the arrhythmia in the treated region is often corrected. Ablation therapy is believed to be more effective than the use of medication in maintaining the heart rhythm. Moreover, the patient does not need a long-term antiarrhythmic medication after ablation procedure. Ablation therapy provides a quick procedure with a high degree of success that does not require open heart surgery (Song & Puskas, 2004).

Radio-frequency (RF) catheter and emerged as an alternative for patients with AF over the past two decades (Song & Puskas, 2004). Many studies have been reported on improving the outcome of radiofrequency ablation for the treatment of AF. The method consists of introducing the catheter into the patient's heart chamber through a major vein. The first step is point-by-point mapping of the left atrium to construct a three-dimensional image of the atrium through the use of a mapping catheter under a fluoroscopy or electroanatomic mapping system. The resulting image is then integrated on the Computed Tomography (CT) or Magnetic Resonance Imaging (MRI) of the patient's atrium (Eckstein et al. 2009).

When the three-dimensional image is constructed, an ablation catheter is positioned in the chamber via the same blood vessel. Radiofrequency energy is then

applied to the metal electrode that is in contact with the arrhythmic substrate to create precise ablation lines that heal to become scar tissue and create insulated barriers in the tissue. The strategic positioning of ablation lines redirects the disorganized signals caused by AF to follow a normal pathway and correct irregular rhythm (Eckstein et al. 2009).

2.6 The Limitations of the Catheter Ablation of Atrial Fibrillation

Although, catheter ablation is the most effective treatment for AF, there are several issues with the procedure. One of the primary concerns is the accuracy of the three-dimensional image constructed by the CT or MRI. The CT or MRI usually is taken a few days prior to the procedure; there are significant differences in the volume of the atrium as determined by the CT or MRI and at the time of the procedure. Since ablation is based on the three-dimensional constructed image. Therefore, the ablation regions are not precise and accurate (Eckstein et al. 2009).

Another concern with the catheter ablation is the identification of the arrhythmogenic foci to be ablated. Current techniques create the lesion lines around the pulmonary veins and on the septal wall of the atrium by dividing the atrium into four sections upon creating the lesion lines thereby redirecting disorganized signals to a normal pathway. Currently there is no technique to identify the arrhythmogenic foci and ablate them directly. In some cases, after the ablation treatment, the arrhythmias come back as a result of inaccurate termination of the arrhythmogenic causing misplaced the ablation regions. The treatment of AF remains mainly based on empirical considerations and is still challenging for the clinicians. Therefore, computer and numerical models have

gained some interest in understanding the mechanism of activation of atrial fibrillation and its behavior.

CHAPTER 3

ELECTRICAL ACTIVITY IN THE HEART

3.1 Introduction

The heart is composed of conduction cells, pacemaker cells, and non-conductive cells. The conduction cells are found in the atria and ventricles tissue that control the heart contractions. The pacemaker cells are self exciting muscle cells and are found in the SA node, AV node, and purkinje fibers. The non-conductive cells are between atria and ventricles walls (Starr & McMillan, 2007).

Contraction of the heart is due to the propagation of electrical impulses through its cells. The cells are arranged in a brick-like structure and are connected to each other through specialized intracellular junctions. These intracellular junctions (gap junctions) are the cell-to-cell electrical pathways and make the connected cells to work as one (Plonsey & Roger, 2007).

The electrical impulses are generated by pacemaker cells, SA node and are propagated through the myocardium (cardiac muscle). Therefore, the stimulated myocardium contracts and causes the heart to beat (Plonsey & Roger, 2007).

3.2 Cardiac Action Potential

Heart cells, like other biological cells have several types of ion channels in cell membranes that interact with each other through their transmembrane potential and capacitance. An action potential is a transient pulse of electrical charges across the cell membrane due to a rapid change in membrane permeability to certain ions. When a muscle cell is in a nonexcited state, the transmembrane potential is referred to as the resting potential. Each cell membrane has a resting transmembrane potential resulting from differences in the ions concentrations on each side of the membrane (extracellular and intracellular). When a cell is stimulated, the inside potential of the cell membrane becomes less negative called depolarization. When a sufficient area of the cell membrane is depolarized, the transmembrane potential increases to a critical level typically known as the threshold potential and remains elevated for a period of time before returning to resting potential. This is called the action potential. The action potential is a stimulus for excitation of adjacent cells and eventually contraction of the myocardium (Chiras, 2005).

The principal ions involved in cardiac action potential are sodium (Na^+), calcium (Ca^{2+}), and potassium (K^+). The intracellular space of all cells has a high concentration of K^+ ions and low concentration of Na^+ ions. Oppositely the concentration of Na^+ ions is high and the concentration of K^+ ions is low in the extracellular fluid. The difference between ion concentrations inside and outside the cells generates a resting transmembrane potential.

The standard mathematical model used for cardiac action potential is the ventricular action potential. Cardiac action potential has 5 phases as shown in FIGURE 3 - 1. When the cell is subjected to a stimulating pacing pulse, several ion channels are activated and K^+ ions diffuse out of the cell in the direction of their concentration gradients while Na^+ ions move into the cell where the Na^+ concentration is low. This process raises the transmembrane potential to its threshold (FIGURE 3 - 1). Once the threshold is reached, additional sodium channels are opened allowing sodium ions to move into the cell while potassium channels get closed. This causes the membrane potential to rise quickly until the peak action potential is reached (Phase 0). By that time the sodium channels begins to close. Due to the decrease in Na^+ permeability action potential amplitude slightly decreases (repolarization) (Phase 1). The small repolarization in Phase 1 is also due to the small movements of K^+ and Ca^{2+} ions. The balance between inward flow of Ca^{2+} and outward flow of K^+ creates Phase 2 of cardiac action potential or plateau phase. At this phase, the membrane action potential is at steady point near to zero. Due to the drop in the membrane potential, the calcium channels close while the potassium channels are still open. The outward movement of K^+ drops the membrane potential below zero and it causes more potassium channels to open. It initiates repolarization again and makes Phase 3. The voltage drops to its original value and remain steady until it is stimulated again (Phase 4) (Kibble & Halsey, 2009).

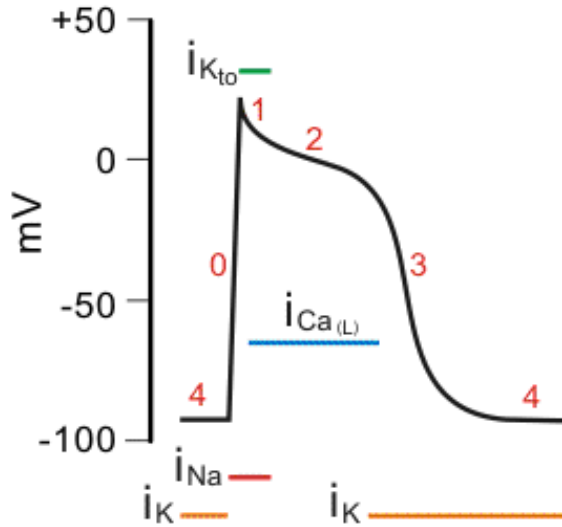


FIGURE 3 - 1 - Ventricular action potential. (Klabunde, 2008) (I_{Na}) refers to Na^+ current, (I_K) refers to potassium current, (I_{to}) refers to transient outward K^+ current, and ($I_{Ca,L}$) refers to the L-type inward Ca^{2+} current.

The atrial action potential is similar to the ventricular action potential. It consists of 5 phases. The only difference is that the plateau phase is longer in ventricular action potential to let the action potential to be spread to all ventricular tissue (Katz, 2006).

The cardiac action potential is generated by the SA node. Cells within the SA node have no true resting potential and generate spontaneous action potential. In SA node action potential, the depolarizing is primarily due to the slow Ca^{2+} currents instead of by fast Na^+ currents. SA node action potential consists of 3 phases (FIGURE 3 - 2) (Klabunde, 2005).

Unlike other action potentials, the depolarization phase of SA node action potential, Phase 0 is created by increase in conductance to Ca^{2+} and decrease in conductance to K^+ . This is then followed by repolarization, Phase 3. In Phase 3, the conductance to Ca^{2+} is decreased and the conductance to K^+ is increased. Once the

membrane potential reaches its threshold, the pacemaker potential will trigger the action potential and depolarization is occurred, Phase 4. In this phase, the K^+ conductance is decrease and the conductance to Ca^{2+} and Na^+ is increased (Klabunde, 2005) (Kibble & Halsey, 2009).

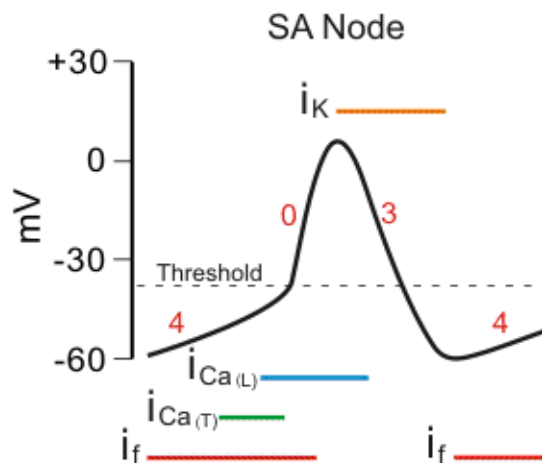


FIGURE 3 - 2 - SA node action potential. (Klabunde, 2008)

3.3 Measurement of Cardiac Electrical Activity (ECG)

The electrical activity of the heart can be measured and recorded on the surface of the body with an electrocardiogram (ECG). A standard ECG has 12 leads that measure the electrical activity of the heart from 12 points. The standard ECG waveforms are illustrated in FIGURE 3 - 3. The ECG waveforms are due to the voltage changes during the myocardium excitation. (Kibble & Halsey, 2009)

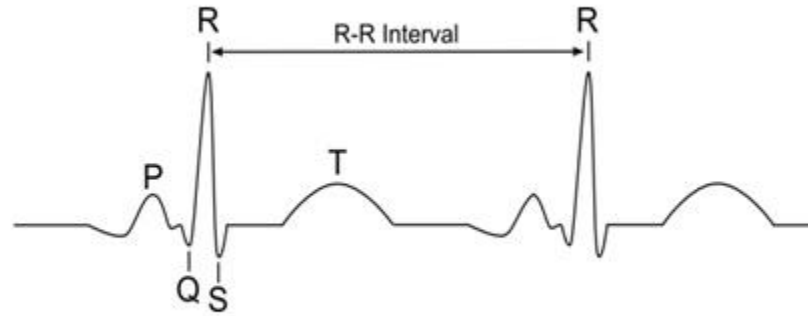


FIGURE 3 - 3 - ECG waves and PR interval. QRS, ST-T, U, T, and P waves are shown. (Enderle et al. 2000)

The atrial depolarization is seen as the P wave on the ECG. The QRS wave represents ventricular depolarization. It is followed by ventricular repolarization that is seen as the ST-T wave on the ECG. (Kibble & Halsey, 2009) The U wave follows T wave with very low amplitude. The duration atrial depolarization is called the PR interval. The QRS interval is the ventricular depolarization duration. The duration of ventricular depolarization and repolarization is called the QT interval. The RR interval represents the ventricular rate; it is the duration of ventricular cardiac cycle (Yanowitz, 2010). The ECG reveals important information about the condition of the heart, heart rate and its rhythm. The ECG is the first step in the heart failure diagnosis.

3.4 Mathematical Modeling of Electrical Activity of the Heart

The field of applied mathematical and computational modeling in physiology has been vastly developed during the last decade and increased the use of models in the

medical industries. Computer modeling has become an essential tool for analyzing experimental data and diagnosing maladies. It provides crucial help for researchers and physicians.

The first computer model of the cardiac action potential was developed by Denis Noble in 1960. The model used Hodgkin-Huxley equation to develop a mathematical model for ion channels (Noble & Hutter, 1960). Since then, many studies have been performed to develop better methods to improve the accuracy of the computer models.

Hodgkin-Huxley is a mathematical model that describes the initiation of action potential in neurons and its propagation. The model evaluates total membrane potential V_m :

$$V_m = -\frac{1}{C_m} \sum I_i \quad (3.1)$$

where C_m is the membrane capacitance, V_m is the membrane potential, and I_i is the ionic current across the membrane obtained by the following equation:

$$I_i = G_i(V_m - E_i) \quad (3.2)$$

where G_i is the conductance of the ion channel and E_i is the equilibrium potential (Plonsey & Roger, 2007).

The Hodgkin-Huxley model was adapted to apply to cardiac action potential by expanding the number of ion channels. Therefore, the mathematical model of action potential in cardiac cell is developed and consequently the action potential propagation in the cardiac tissue can be obtained.

CHAPTER 4

ATRIAL TISSUE MODEL

4.1 Introduction

One of the main factors impeding studies of atrial fibrillation mechanism and its therapy is the absence of a sufficient model to provide usable data (Kijawornrat et al. 2008). The recent development of the atrial tissue models with the more realistic anatomic structure provides an essential tool in the analysis of atrial arrhythmias.

In order to develop a proper model of electrical activity in cardiac tissue, the current flow needs to be modeled within and between cells, across the cell membrane, and in the extracellular medium. The cell model consists of ion concentration, membrane potential, and transmembrane ionic current. The tissue model includes the cell interconnections and the overall geometric structure of the tissue.

There are several models based on membrane ionic channel kinetics for atrial cell (Courtemanche et al. 1998). There are a number of factors to consider in the selection of a single cell model such as the computer power availability and the degree of accuracy desired (Cherry et al. 2000). In this project, the Courtemanche et al. model has been used; it is developed specifically for atrial cells (Courtemanche et al. 1998).

4.2 Courtemanche et al. Cell Model

There are two mathematical ionic models published for human atrial cells model. One is the Nygren, et al. model with 30 variables and the other one is the Courtemanche et al. model with 21 variables (Courtemanche et al. 1998) (Nygren, et al., 1998). These models are capable of reproducing different action potential behaviors. Using these models, the role of different currents in atrial fibrillation can be investigated.

In this research, the Courtemanche et al. model is used to mathematically model the human atrial action potential, based on the K^+ , Na^+ and Ca^{2+} currents (Courtemanche et al. 1998). The tissue model is driven from the cell model by a finite element method.

In the Courtemanche et al. model, the cell membrane is represented by a capacitor connected in parallel with variable resistances representing the ionic channels and batteries representing driving forces. The changes in membrane potential is given by

$$\frac{dV}{dt} = \frac{-(I_{ion} + I_{st})}{C_m} \quad (4.1)$$

where I_{ion} is the total ionic current in picoamperes per picofarad, I_{st} is the stimulus current, C_m is the total membrane capacitance in picofarads per unit area, V is the membrane potential in millivolts and time (t) is in milliseconds (Courtemanche et al. 1998).

In the Courtemanche et al. model, the total ionic current is given by

$$I_{ion} = I_{Na} + I_{K1} + I_{to} + I_{Kur} + I_{Kr} + I_{Ks} + I_{Ca,L} + I_{p,ca} + I_{NaK} + I_{NaCa} + I_{b,Na} + I_{b,ca} \quad (4.2)$$

In this expression, the total ionic current takes into account the fast Na^+ current (I_{Na}), the time-dependent K^+ current (I_{K1}), the transient outward K^+ current (I_{to}), the

ultra-rapid delayed rectifier K^+ current (I_{Kur}), the rapid delayed rectifier K^+ current (I_{Kr}), the slow delayed rectifier K^+ current (I_{Ks}), the L-type inward Ca^{2+} current ($I_{Ca,L}$), the sarcoplasmic Ca^{2+} pump current ($I_{p,Ca}$), the Na^+ - K^+ pump current (I_{NaK}), the Na^+ - Ca^{2+} exchanger current (I_{NaCa}), the background Na^+ current ($I_{b,Na}$), the background Ca^{2+} current ($I_{b,Ca}$) (Courtemanche et al. 1998).

The model tracks the intracellular concentrations $[Na^+]$, $[Ca^{2+}]$, and $[K^+]$, and the handling of intracellular $[Ca^{2+}]$ concentration by the sarcoplasmic reticulum system (SR). The extracellular ion concentrations are kept to be fixed here. The membrane capacitance is $C_m = 1 \mu F/cm^2$ (Courtemanche et al. 1998).

The intracellular compartment is the sarcoplasmic reticulum (SR), which is divided into two sub-compartments: the network SR (NSR) and the junctional SR (JSR). The schematic diagram of the cell model is shown in FIGURE 4 - 1 (Courtemanche et al. 1998).

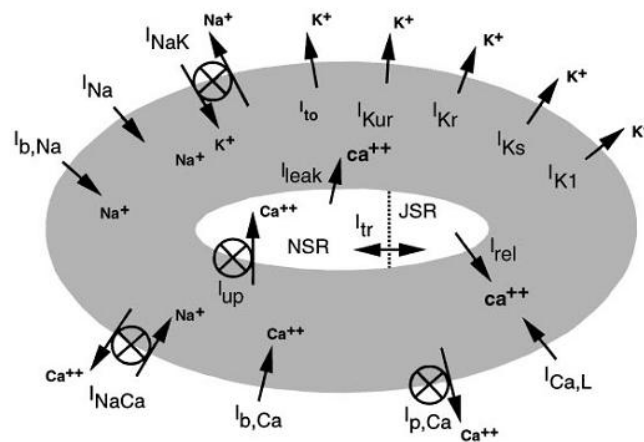


FIGURE 4 - 1 - Schematic diagram of the cell model. The diagram represents ionic currents, pumps, and exchangers. The intracellular compartments are myoplasm, sarcoplasmic reticulum (SR) consisting junctional SR (JSR)[release compartment], and network SR (NSR) [uptake compartment] (Courtemanche et al. 1998).

In this model, the intracellular concentrations $[Na^+]$, $[K^+]$, and $[Ca^{2+}]$ are given by the following equations:

$$\frac{d[Na^+]_i}{dt} = \frac{-3I_{NaK} - 3I_{NaCa} - I_{b,Na} - I_{Na}}{FV_i} \quad (4.3)$$

$$\frac{d[K^+]_i}{dt} = \frac{2I_{NaK} - I_{K1} - I_{to} - I_{Kur} - I_{Kr} - I_{Ks} - I_{b,K}}{FV_i} \quad (4.4)$$

$$\frac{d[Ca^{2+}]_i}{dt} = \frac{\left[\frac{2I_{NaCa} - I_{p,Ca} - I_{Ca,L} - I_{b,Ca}}{2FV_i} + \frac{V_{up}(I_{up,leak} - I_{up}) + I_{rel}V_{rel}}{V_i} \right]}{\left[1 + \frac{[Trpn]_{max}K_{m,Trpn}}{([Ca^{2+}]_i + K_{m,Trpn})^2} + \frac{[Cmdn]_{max}K_{m,Cmdn}}{([Ca^{2+}]_i + K_{m,Cmdn})^2} \right]} \quad (4.5)$$

where $[X]_i$ is the intracellular concentration of ion i , F is the Faraday constant, V_i is the intracellular volume, V_{up} is the SR uptake compartment volume, $I_{up,leak}$ is the Ca^{2+} leak current from the NSR, I_{up} is the Ca^{2+} uptake current into the NSR, I_{rel} is the Ca^{2+} release current from the JSR, V_{rel} is the SR release compartment volume, $[Trpn]_{max}$ is the total troponin concentration in myoplasm, $K_{m,Trpn}$ is the Ca^{2+} half-saturation constant for troponin, $[Cmdn]_{max}$ is the total calmodulin concentration in myoplasm, $K_{m,Cmdn}$ is the Ca^{2+} half-saturation constant for calmodulin (Courtemanche et al. 1998).

The uptake and release concentration of Ca^{2+} by sarcoplasmic reticulum are given by:

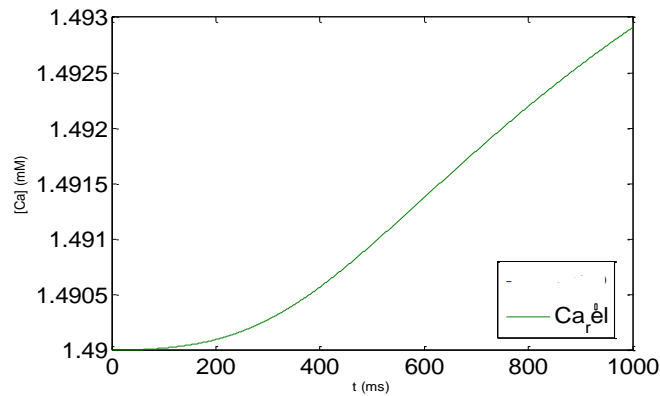
$$\frac{d[Ca^{2+}]_{up}}{dt} = I_{up} - I_{up,leak} - I_{tr} \frac{V_{rel}}{V_{up}} \quad (4.6)$$

$$\frac{d[Ca^{2+}]_{rel}}{dt} = (I_{tr} - I_{rel}) \left\{ 1 + \frac{[Csqn]_{max}K_{m,Csqn}}{([Ca^{2+}]_{rel} + K_{m,Csqn})^2} \right\}^{-1} \quad (4.7)$$

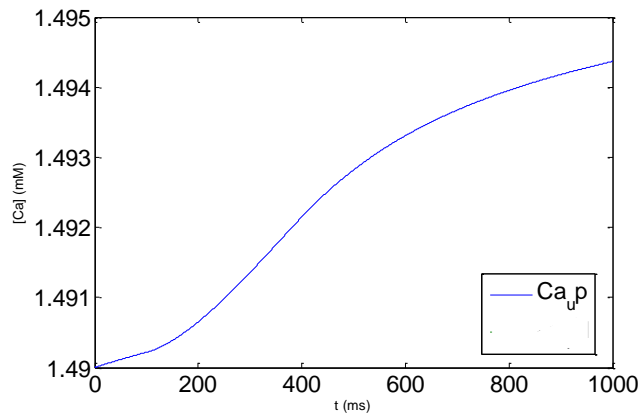
where $[Ca^{2+}]_{up}$ and $[Ca^{2+}]_{rel}$ are Ca^{2+} concentration in uptake and release compartment, respectively, I_{up} is the Ca^{2+} uptake current into NSR, $I_{up,leak}$ is the Ca^{2+} leak current form the NSR, I_{tr} is the Ca^{2+} transfer current from NSR to JSR, V_{rel} and V_{up} are the SR release and uptake compartment volumes, respectively, I_{rel} is the Ca^{2+} release current form JSR,

$[Csqn]_{max}$ is the total calsequestrin concentration in JSR, $K_{m,Csqn}$ is the Ca^{2+} half saturation constant for calsequestrin (Courtemanche et al. 1998).

The ionic concentrations were solved with Euler's method in the Courtemanche et al. model. In this research, all the ionic concentrations and gating parameters are solved with Matlab using the Runge-Kutta (4,5) integration method. The results are shown in FIGURE 4 - 2.

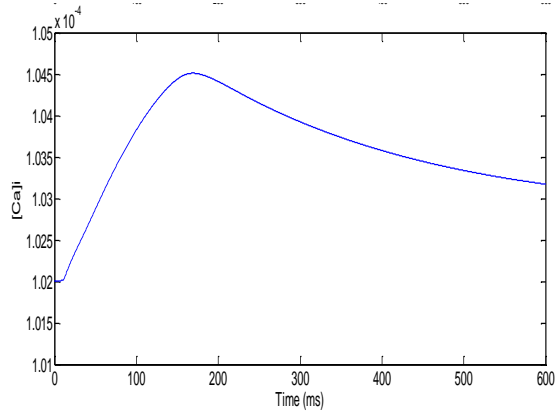


A) $[Ca^{2+}]_{rel}$ concentration

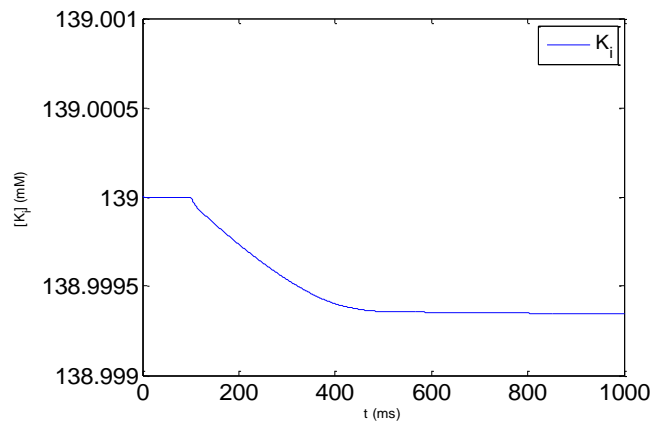


B) $[Ca^{2+}]_{up}$ concentration

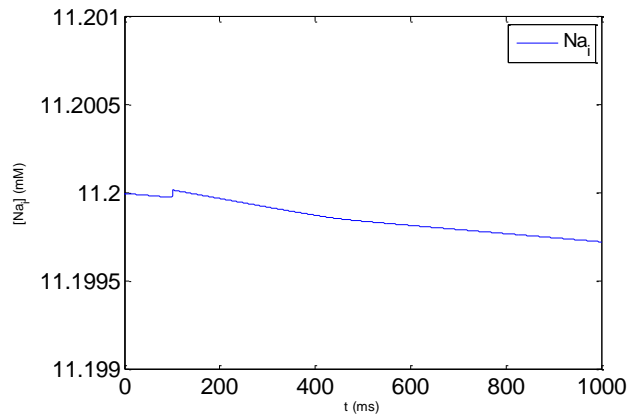
FIGURE 4 - 2 - Ionic concentrations variable obtained with the Runge-Kutta (4,5) integration method.



C) $[Ca^{2+}]_i$ concentration



D) $[K^+]_i$ concentration



E) $[Na^+]_i$ concentration

FIGURE 4 - 2 - (Continued)

As FIGURE 4 - 2 shows, when stimulus current is applied, there is a slow inward movement of Ca^{2+} to a max point where it represents Phase 2 of AP and then decreases as AP enters Phase 3 and the L-type Ca^{2+} channels close. Intracellular K^+ concentration starts decreasing when an impulse is applied due to the outward movement of K^+ through the Phase 1 to 4. Na^+ concentration has a sharp rise since the excitation opens the fast Na^+ channels and causes influx of Na^+ ions. The inactivation of the fast Na^+ channels creates Phase 1 of AP.

In the Courtemanche et al. model, cell compartment volumes are based on Luo and Rudy model. According to Luo and Rudy, the volume fraction of SR (FSR) is modeled at 6% of the cell volume. The SR volume is then divided into JSR (8%) and NSR (92%). Therefore, the volume fraction of JSR is $0.48\% = 8\% * 6\%$ and the volume fraction of NSR is $5.52\% = 92\% * 6\%$ of the cell volume. The mitochondria volume fraction is set at 26% (Schaper et al. 1985). The remaining volume is the fraction of myoplasm at 68%. In the stated model, the fraction volume of the cell and cleft is assumed to be 88% and 12%, respectively (Forbes & Sperelakis, 1989) (Gerdes & Kasten, 1980) (Severs et al. 1985).

Ionic currents in the Courtemanche et al. model are based on the equilibrium potential of ion X (E_x) and the maximal conductance of ion X (g_x). The equilibrium potential is given by Nernst equation:

$$E_x = \frac{RT}{zF} \log \frac{[X]_e}{[X]_i} \quad (4.8)$$

where R is the gas constant, T is the temperature, $z = 1$ for Na^+ and K^+ , $z = 2$ for Ca^{2+} , F is the Faraday constant, $[X]_e$ is the extracellular concentration of ion X and $[X]_i$ is the

intracellular concentration of ion X. The extracellular concentrations are assumed to be constant in this model (Courtemanche et al. 1998).

4.2.1 Fast Na⁺ Current

The large and rapid inward Na⁺ current is the major responsible current of the depolarization phase at the beginning of the action potential. The current is given by

$$I_{Na} = g_{Na} m^3 h j (V - E_{Na}) \quad (4.9)$$

where m, h, and j are gating variable and are calculated using equation (4.9). V is the transmembrane potential and $g_{Na} = 7.8$ nS/pF (Courtemanche et al. 1998).

$$\frac{dy}{dt} = \frac{y_{\infty} - y}{\tau_y} \quad (4.10)$$

where y is any gating variable

$$\tau_{\phi} = (\alpha_{\phi} + \beta_{\phi})^{-1}, \quad \phi_{\infty} = \alpha_{\phi} \tau_{\phi}, \quad \text{for } \phi = m, h, j \quad (4.11)$$

The coefficients of gating variables m, h, and j are given by:

$$\alpha_m = \begin{cases} 0.32 \frac{V+47.13}{1-\exp[-0.1(V+47.13)]} \\ 3.2, & \text{if } V \geq -47.13 \end{cases} \quad (4.12)$$

$$\beta_m = 0.08 \exp\left(-\frac{V}{11}\right) \quad (4.13)$$

$$\alpha_h = \begin{cases} 0.135 \exp\left(-\frac{V+80}{6.8}\right) \\ 0, & \text{if } V \geq -40 \end{cases} \quad (4.14)$$

$$\beta_h = \begin{cases} 3.56 \exp(0.079 V) + 3.1 \times 10^5 \exp(0.35 V) \\ \{0.13 [1 + \exp\left(-\frac{V+10.66}{11.1}\right)]\}, & \text{if } V \geq -40 \end{cases} \quad (4.15)$$

$$\alpha_j = \begin{cases} [-127,140 \exp(0.2444V) - 3.474 \times 10^{-5} \exp(-0.04391 V)] \frac{V + 37.78}{1 + \exp[0.311 (V + 79.23)]} \\ 0, & \text{if } V \geq -40 \end{cases} \quad (4.16)$$

$$\beta_j = \begin{cases} 0.1212 \frac{\exp(-0.01052 V)}{1 + \exp[-0.1378 (V + 40.14)]} \\ 0.3 \frac{\exp[-2.535 \times 10^{-7} V]}{1 + \exp[-0.1 (V + 32)]}, & \text{if } V \geq -40 \end{cases} \quad (4.17)$$

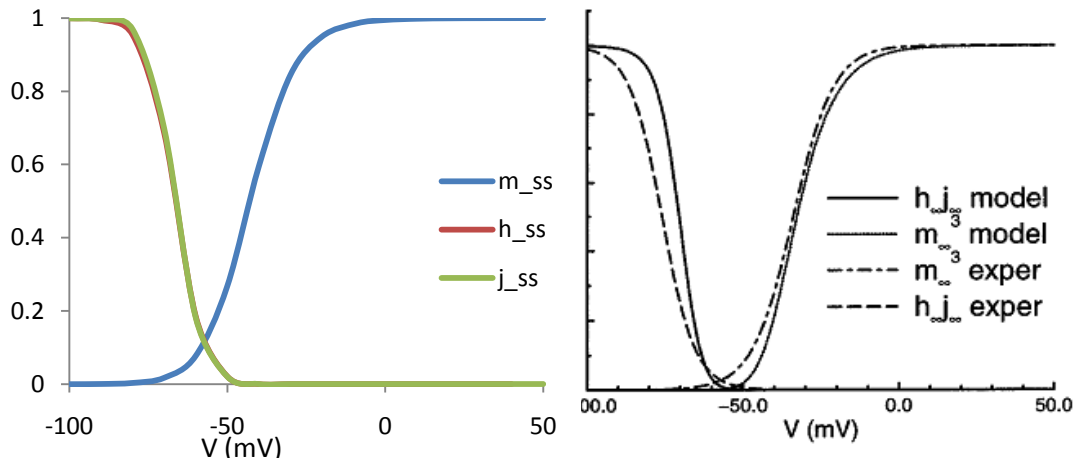


FIGURE 4 - 3 - Steady state activation and inactivation curves of the fast Na^+ channel parameters. The data given in the Courtemanche et al. report is shown on the left figure (Courtemanche et al. 1998).

In the Courtemanche et al. model direct integration was used to solve all the gating variables (Courtemanche et al. 1998). In this report, gating variables are solved in a system of ODEs by Matlab using the Runge-Kutta (4,5) integration method. FIGURE 4 - 4 shows the gating parameters of the fast Na^+ . The gating variables change in 0 to 1 range, close to open state respectively.

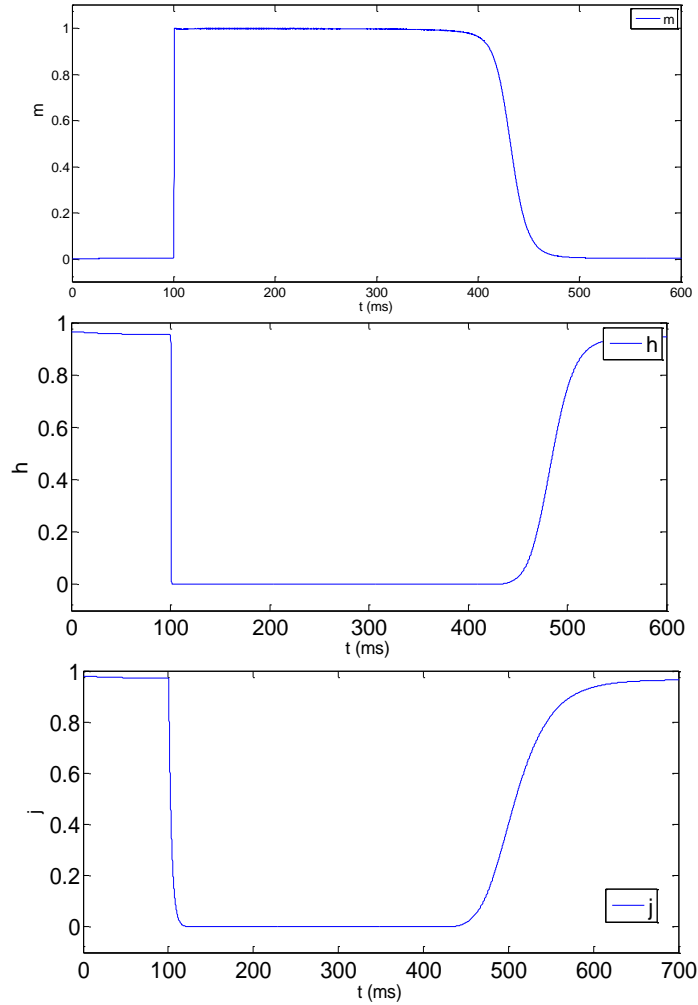


FIGURE 4 - 4 - Gating parameter variables of the fast Na^+ channel with the Runge-Kutta (4,5) integration method.

The fast Na^+ current is shown in FIGURE 4 - 5.

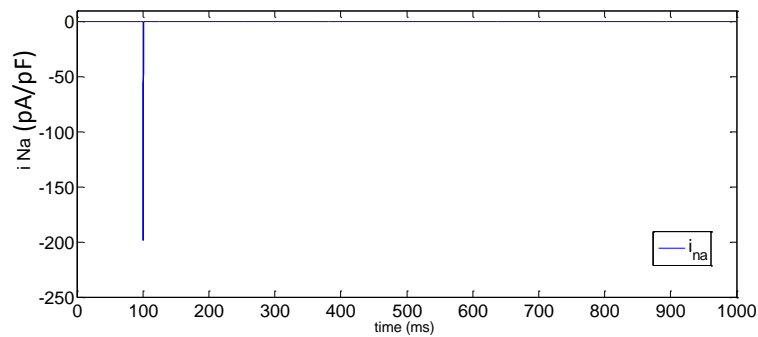


FIGURE 4 - 5 - The fast Na^+ current in a period of 1000 ms and stimulus current at 100ms.

4.2.2 Time-Dependent K⁺ Current

K⁺ current is significant in determining resting membrane potential and resistance and plays an important role in the late repolarization phase of action potential. The current is given by:

$$I_{K1} = \frac{g_{K1}(V-E_K)}{1+\exp[0.07(V+80)]} \quad (4.18)$$

where $g_{K1} = 0.09$ nS/pF (Courtemanche et al. 1998).

Time-dependent K⁺ current is shown in FIGURE 4 - 6.

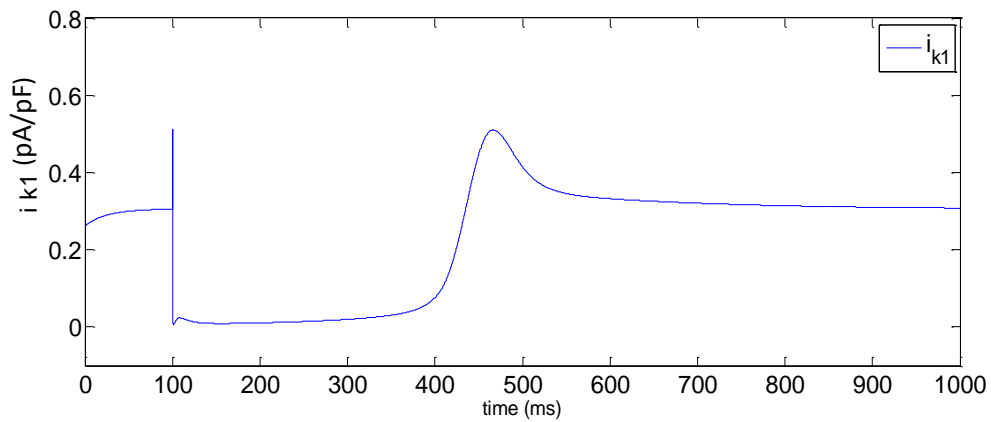


FIGURE 4 - 6 - Time-dependent K⁺ current in a period of 1000 ms and stimulus current at 100 ms.

4.2.3 Transient Outward K⁺ Current

Transient Outward K⁺ current is given by:

$$I_{to} = g_{to} o_a^3 o_i (V - E_K) \quad (4.19)$$

where O_a and O_i are gating variables and are calculated using equation (4.9), and $g_{to}=0.1652$ nS/pF (Courtemanche et al. 1998).

The coefficients of gating variables are given by:

$$\tau_{o(a)} = [\alpha_{o(a)} + \beta_{o(a)}]^{-1}/K_{Q10} \quad (4.20)$$

$$\alpha_{o(a)} = 0.65 \left[\exp\left(-\frac{V+10}{8.5}\right) + \exp\left(-\frac{V-30}{59.0}\right) \right]^{-1} \quad (4.21)$$

$$\beta_{o(a)} = 0.65 \left[2.5 + \exp\left(\frac{V+82}{17.0}\right) \right]^{-1} \quad (4.22)$$

$$o_{a(\infty)} = \left[1 + \exp\left(-\frac{V+20.47}{17.54}\right) \right]^{-1} \quad (4.23)$$

$$\tau_{o(i)} = [\alpha_{o(i)} + \beta_{o(i)}]^{-1}/K_{Q10} \quad (4.24)$$

$$\alpha_{o(i)} = \left[18.53 + \exp\left(\frac{V+113.7}{10.95}\right) \right]^{-1} \quad (4.25)$$

$$\beta_{o(i)} = \left[35.58 + \exp\left(-\frac{V+1.26}{7.44}\right) \right]^{-1} \quad (4.26)$$

$$o_{i(\infty)} = \left[1 + \exp\left(\frac{V+43.1}{5.3}\right) \right]^{-1} \quad (4.27)$$

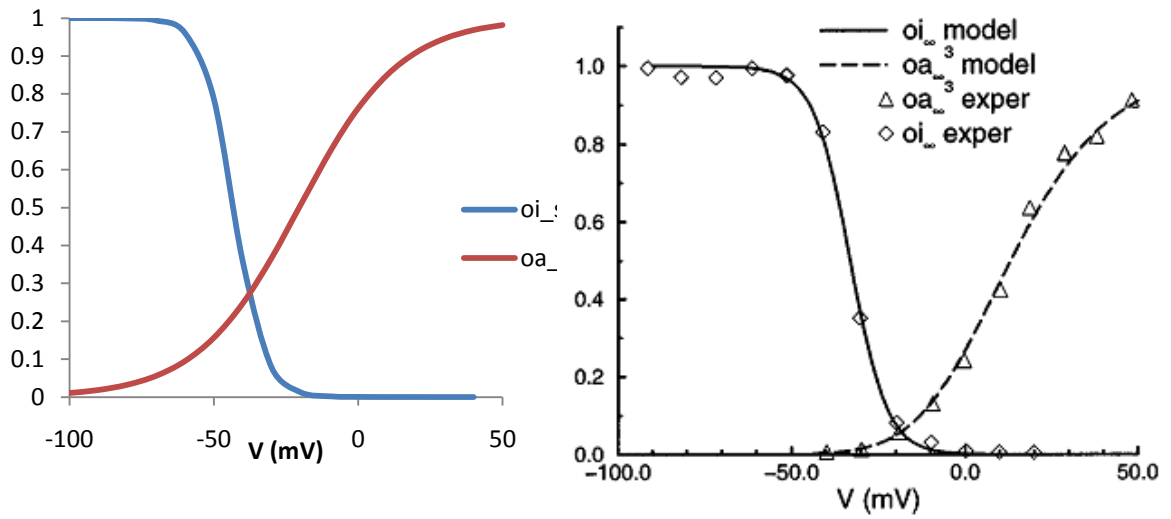


FIGURE 4 - 7 - Steady state activation and inactivation curves of the transient outward K^+ current parameters. The data given in the Courtemanche et al. report is shown on the left figure (Courtemanche et al. 1998).

K_{Q10} is the temperature adjustment factor, $K_{Q10} = 3$ (Courtemanche et al. 1998).

FIGURE 4 - 8 shows the gating parameters of the transient outward K^+ current using the Runge-Kutta (4,5) integration method.

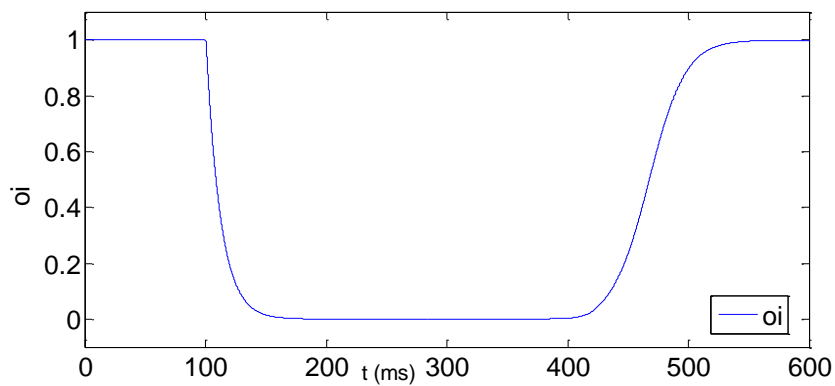


FIGURE 4 - 8 - Gating parameter variables of the transient outward K^+ current at a period of 1000 ms.

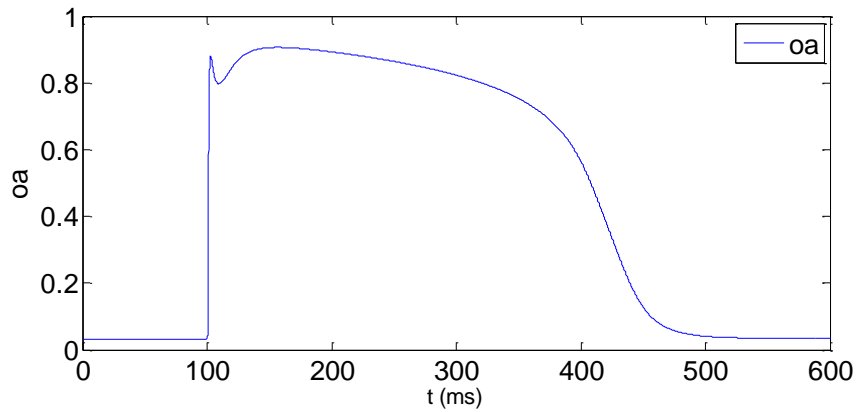


FIGURE 4 - 8 - (Continued)

The transient outward K^+ current is shown in FIGURE 4 - 9. The current increases with stimulus current and then slowly decreases to zero. The current plays an important role in Phase 1 and 2 of AP. The result is in agreement with data from Courtemanche et al (Courtemanche et al. 1998).

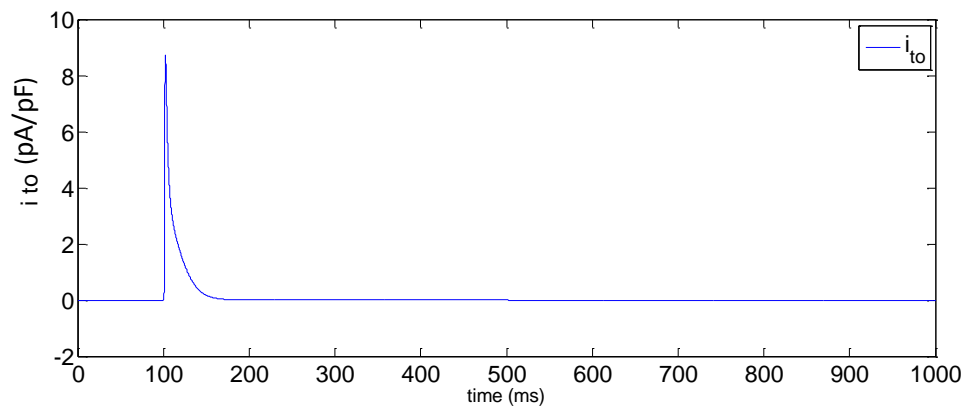


FIGURE 4 - 9 - Transient outward K^+ current in a period of 1000 ms and stimulus current at 100 ms.

4.2.4 Ultrarapid Delayed Rectifier K^+ Current

This current is given by:

$$I_{Kur} = g_{Kur} u_a^3 u_i (V - E_K) \quad (4.28)$$

where u_a and u_i are gating variables and are calculated using equation (4.9), and g_{Kur} is given by:

$$g_{Kur} = 0.005 + \frac{0.05}{1 + \exp\left[\frac{(V-15)}{-13}\right]} \quad (4.29)$$

The coefficients of gating variables are given by:

$$\tau_{u(a)} = [\alpha_{u(a)} + \beta_{u(a)}]^{-1} / K_{Q10} \quad (4.30)$$

$$\alpha_{u(a)} = 0.65 \left[\exp\left(-\frac{V+10}{8.5}\right) + \exp\left(-\frac{V-30}{59.0}\right) \right]^{-1} \quad (4.31)$$

$$\beta_{u(a)} = 0.65 \left[2.5 + \exp\left(\frac{V+82}{17.0}\right) \right]^{-1} \quad (4.32)$$

$$u_{a(\infty)} = \left[1 + \exp\left(-\frac{V+30.3}{9.6}\right) \right]^{-1} \quad (4.33)$$

$$\tau_{u(i)} = [\alpha_{u(i)} + \beta_{u(i)}]^{-1} / K_{Q10} \quad (4.34)$$

$$\alpha_{u(i)} = \left[21 + \exp\left(-\frac{V-185}{28}\right) \right]^{-1} \quad (4.35)$$

$$\beta_{u(i)} = \exp\left(\frac{V-158}{16}\right) \quad (4.36)$$

$$u_{i(\infty)} = \left[1 + \exp\left(\frac{V-99.45}{27.48}\right) \right]^{-1} \quad (4.37)$$

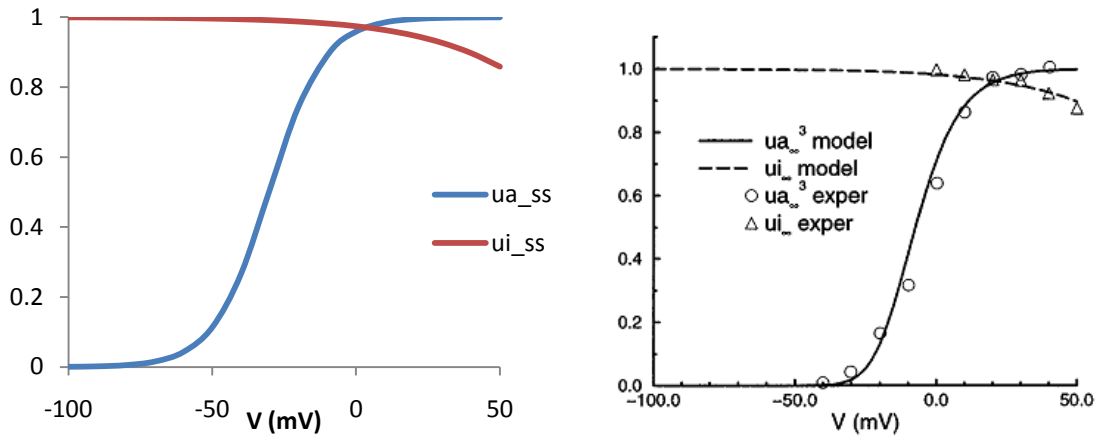


FIGURE 4 - 10 - Steady state activation and inactivation curves of the ultrarapid delayed rectifier K⁺ current parameters. The data given in the Courtemanche et al. report is shown on the left figure (Courtemanche et al. 1998).

FIGURE 4 - 11 shows the gating parameters of the ultrarapid delayed rectifier K⁺ current solved with the Runge-Kutta (4,5) integration method.

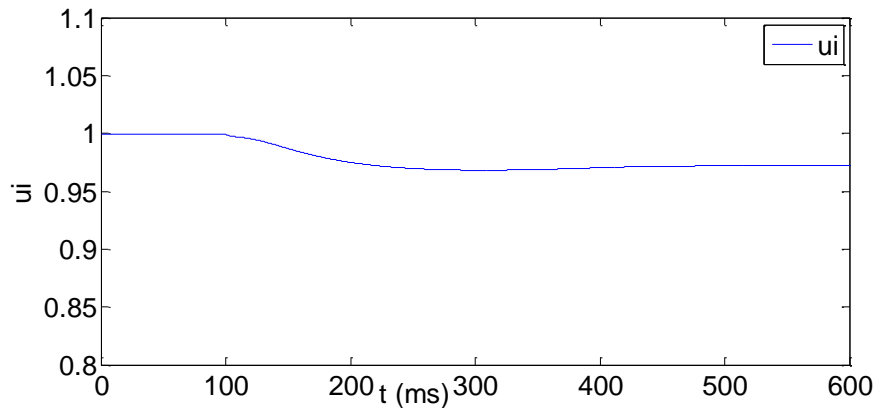


FIGURE 4 - 11 - Gating parameter variables of the ultrarapid delayed rectifier K⁺ current at a period of 1000 ms.

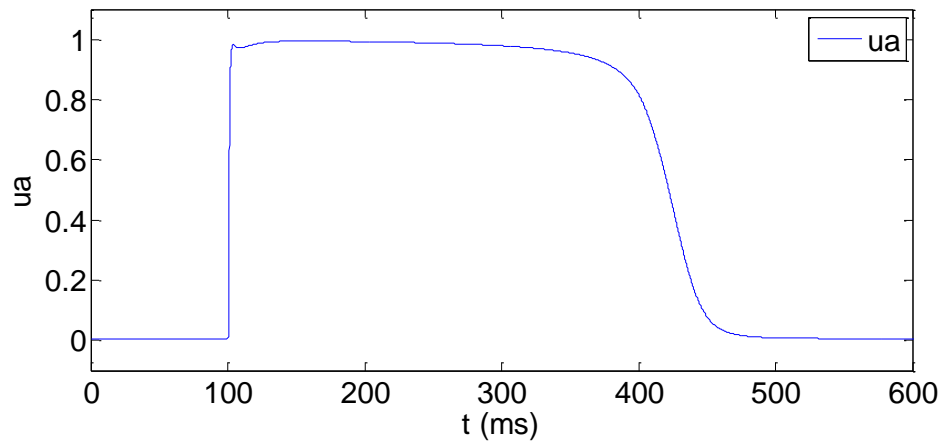


FIGURE 4 - 11 - (Continued)

The ultrarapid delayed rectifier K^+ current calculated using the Runge-Kutta (4,5) integration method is shown in FIGURE 4 - 12.

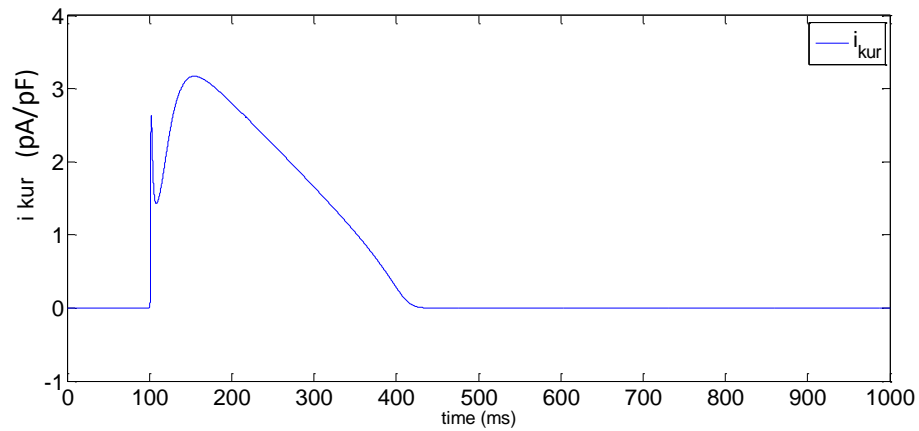


FIGURE 4 - 12 - Ultrarapid delayed rectifier K^+ current in a period of 1000 ms and stimulus current at 100 ms.

4.2.5 Rapid Delayed Rectifier K⁺ Current

This current is given by:

$$I_{Kr} = \frac{g_{Kr}x_r(V-E_K)}{1+\exp(\frac{V+15}{22.4})} \quad (4.38)$$

where $g_{Kr} = 0.0294$ and x_r is gating variable (Courtemanche et al. 1998), which satisfies equation (4.9) with the following coefficients:

$$\tau_{x(r)} = [\alpha_{x(r)} + \beta_{x(r)}]^{-1} \quad (4.39)$$

$$\alpha_{x(r)} = 0.0003 \frac{V+14.1}{1-\exp(-\frac{V+14.1}{5})} \quad (4.40)$$

$$\beta_{x(r)} = 7.3898 \times 10^{-5} \frac{V-3.3328}{\exp(\frac{V-3.3328}{5.1237})-1} \quad (4.41)$$

$$x_{r(\infty)} = [1 + \exp(-\frac{V+14.1}{6.5})]^{-1} \quad (4.42)$$

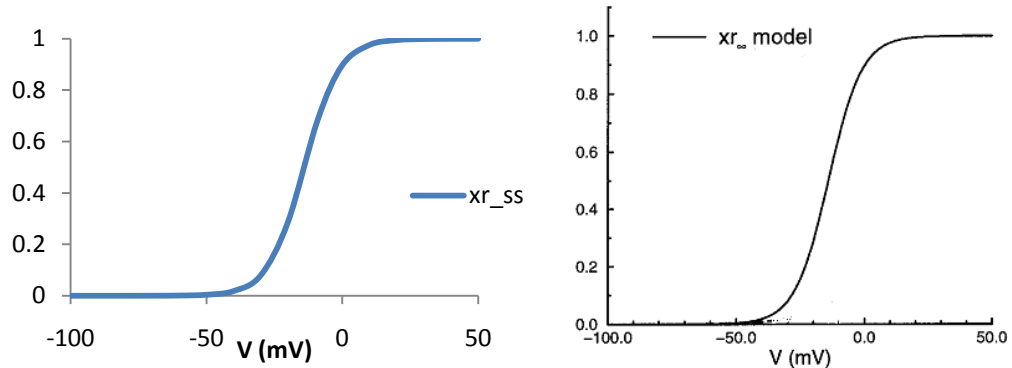


FIGURE 4 - 13 - Steady state activation and inactivation curves of the rapid delayed rectifier K⁺ current parameter. The data given in the Courtemanche et al. report is shown on the left figure (Courtemanche et al. 1998).

FIGURE 4 - 14 shows the gating parameter of the rapid delayed rectifier K^+ current solved using the Runge-Kutta (4,5) integration method. The result is in agreement with the result from the Courtemanche et al. model (Courtemanche et al. 1998).

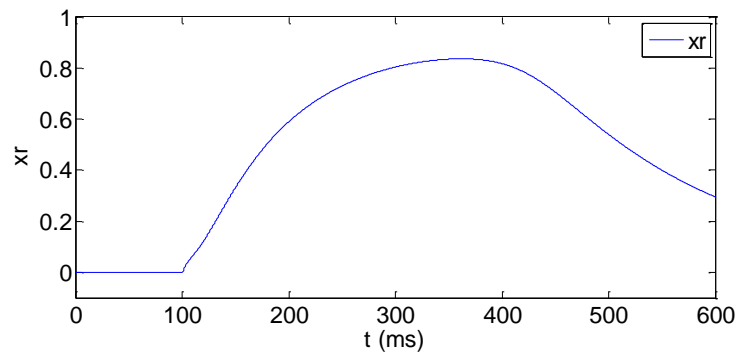


FIGURE 4 - 14 - Gating parameter variables of the rapid delayed rectifier K^+ current at a period of 1000 ms.

The rapid delayed rectifier K^+ current calculate using the Runge-Kutta (4,5) integration method is shown in FIGURE 4 - 15.

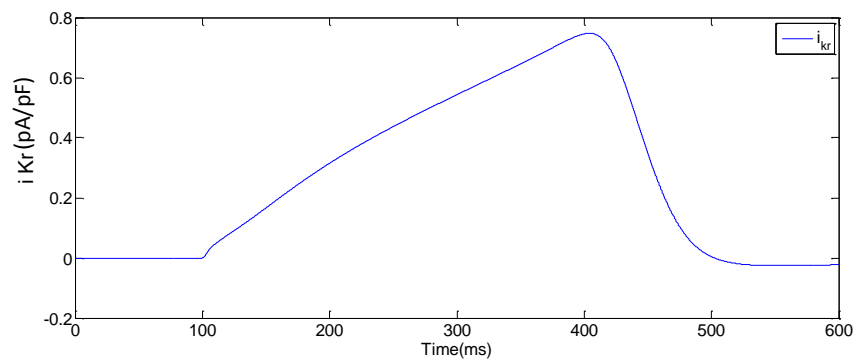


FIGURE 4 - 15 - Rapid delayed rectifier K^+ current in a period of 1000 ms and stimulus current at 100 ms.

4.2.6 Slow Delayed Rectifier K⁺ Current

This current is given by:

$$I_{Ks} = g_{Ks} x_s^2 (V - E_K) \quad (4.43)$$

where $g_{Ks} = 0.129$ and x_s is a gating variable (Courtemanche et al. 1998), which satisfies equation (4.9) with the following coefficients:

$$\tau_{x(s)} = \frac{1}{2} [\alpha_{x(s)} + \beta_{x(s)}]^{-1} \quad (4.44)$$

$$\alpha_{x(s)} = 4 \times 10^{-5} \frac{V-19.9}{1 - \exp(-\frac{V-19.9}{17})} \quad (4.45)$$

$$\beta_{x(s)} = 3.5 \times 10^{-5} \frac{V-19.9}{\exp(\frac{V-19.9}{9}) - 1} \quad (4.46)$$

$$x_{s(\infty)} = [1 + \exp(-\frac{V-19.9}{12.7})]^{-\frac{1}{2}} \quad (4.47)$$

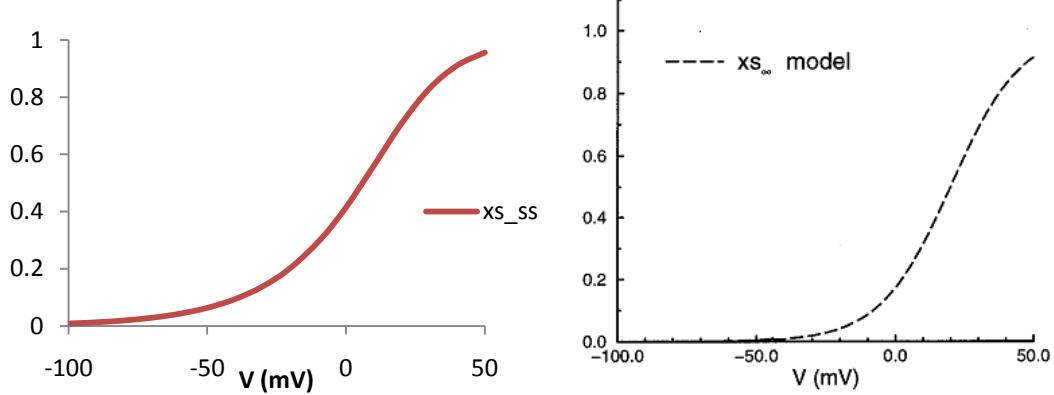


FIGURE 4 - 16 - Steady state activation and inactivation curves of the slow delayed rectifier K⁺ current parameter. The data given in the Courtemanche et al. report is shown on the left figure (Courtemanche et al. 1998).

FIGURE 4 - 17 shows the gating parameter of the slow delayed rectifier K⁺ current solved by the Runge-Kutta (4,5) integration method.

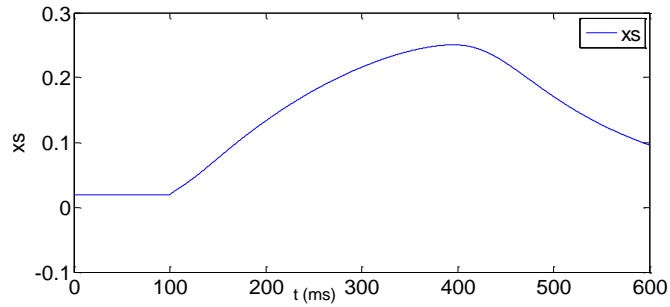


FIGURE 4 - 17 - Gating parameter variables of the slow delayed rectifier K⁺ current at a period of 1000 ms.

The slow delayed rectifier K⁺ current calculated using the Runge-Kutta (4,5) integration method is shown in FIGURE 4 - 18.

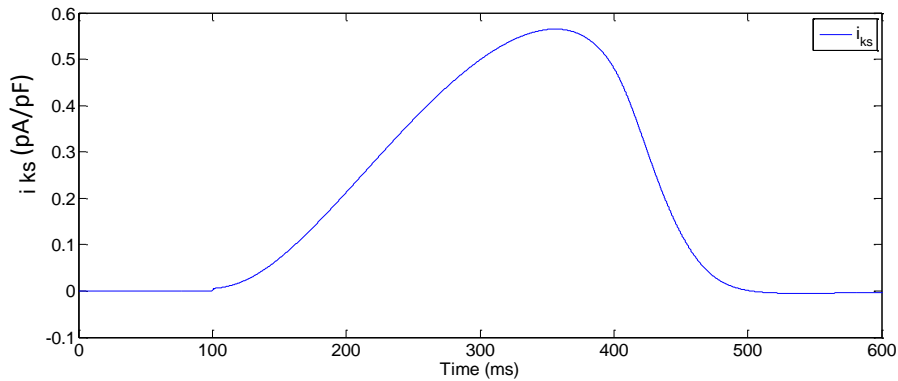


FIGURE 4 - 18 -Slow delayed rectifier K⁺ current in a period of 1000 ms and stimulus current at 100 ms.

4.2.7 L-Type Inward Ca²⁺ Current

The L-type inward Ca²⁺ current is given by:

$$I_{Ca,L} = g_{Ca,L} d f f_{Ca}(V - 65) \quad (4.48)$$

where $g_{Ca,L} = 0.1238$ and d , f , and f_{Ca} are gating variables (Courtemanche et al. 1998), which satisfies the equation (4.9) where y is any of d , f , or f_{Ca} with the following coefficients:

$$\tau_d = \frac{1 - \exp\left(-\frac{V+10}{6.24}\right)}{0.035 (V+10) [1 + \exp\left(-\frac{V+10}{6.24}\right)]} \quad (4.49)$$

$$d_\infty = \left[1 + \exp\left(-\frac{V+10}{8}\right)\right]^{-1} \quad (4.50)$$

$$\tau_f = 9 \{0.0197 \exp[-0.0337^2 (V + 10)^2] + 0.02\}^{-1} \quad (4.51)$$

$$f_\infty = \left[1 + \exp\left(\frac{V+28}{6.9}\right)\right]^{-1} \quad (4.52)$$

$$\tau_{f(Ca)} = 2, \quad f_{Ca(\infty)} = \left(1 + \frac{[Ca^{2+}]_i}{0.00035}\right)^{-1} \quad (4.53)$$

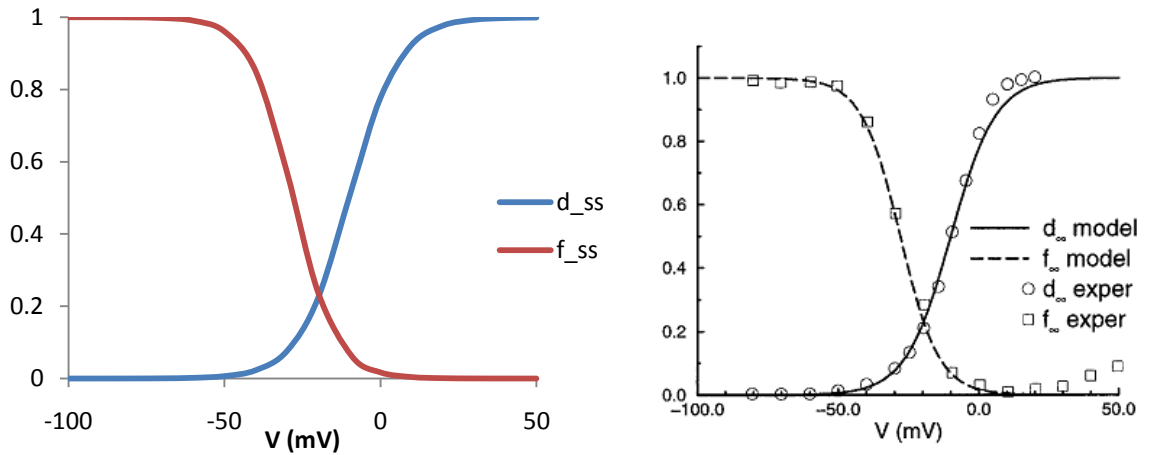


FIGURE 4 - 19 - Steady state activation and inactivation curves of the L-type inward Ca²⁺ current parameters. The data given in the Courtemanche et al. report is shown in the left figure (Courtemanche et al. 1998).

FIGURE 4 - 20 shows the L-type inward Ca^{2+} current solved by the Runge-Kutta (4,5) integration method. The result is in agreement with result from Courtemanche et al.

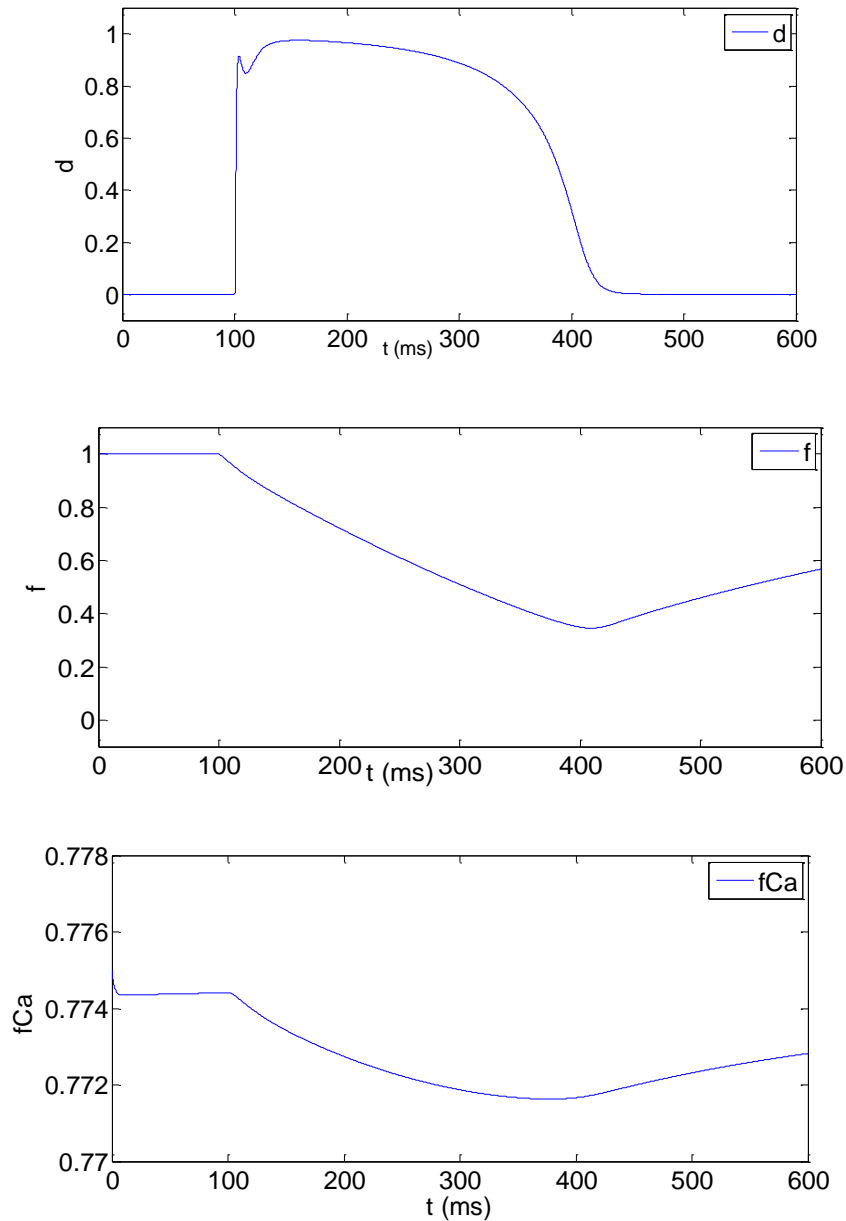


FIGURE 4 - 20 - Gating parameter variables of the L-type inward Ca^{2+} current at a period of 1000 ms.

The L-type inward Ca^{2+} current calculated using the Runge-Kutta (4,5) integration method is shown in FIGURE 4 - 21.

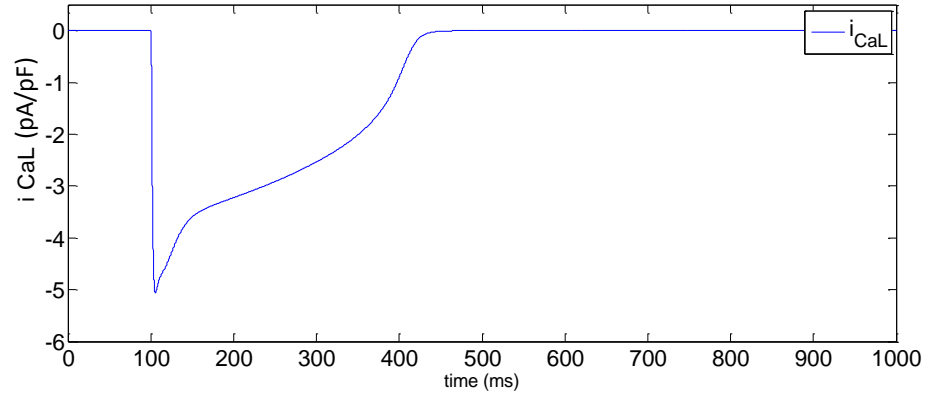


FIGURE 4 - 21 - L-type inward Ca^{2+} current in a period of 1000 ms and stimulus current at 100 ms.

4.2.8 Ca^{2+} Pump Current

The current is given by:

$$I_{p,ca} = I_{p,ca(\max)} \frac{[\text{Ca}^{2+}]_i}{0.0005 + [\text{Ca}^{2+}]_i} \quad (4.54)$$

where according to the Courtemanche et al. model, $I_{p,ca(\max)} = 0.275$ (Courtemanche et al. 1998).

The Ca^{2+} pump current calculated using the Runge-Kutta (4,5) integration method is shown in FIGURE 4 - 22.

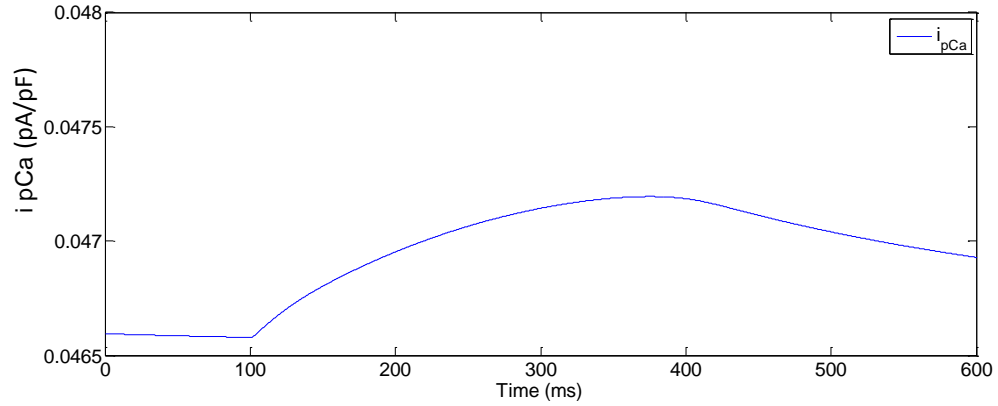


FIGURE 4 - 22 - Ca²⁺ pump current in a period of 1000 ms and stimulus current at 100 ms.

4.2.9 Na⁺ - K⁺ Pump Current

This current is given by:

$$I_{NaK} = I_{NaK(max)} f_{NaK} \frac{1}{1 + \left\{ \frac{K_{m,Na(i)}}{[Na^+]_i} \right\}^{1.5}} \frac{[K^+]_o}{[K^+]_o + K_{m,K(o)}} \quad (4.55)$$

where $I_{NaK(max)} = 0.6$, $K_{m,Na(i)}$ and $K_{m,K(o)}$ are the $[Na^+]_i$ and $[K^+]_o$ half saturation constants, respectively (Courtemanche et al. 1998). f_{NaK} is given by:

$$f_{NaK} = [1 + 0.1245 \exp(-0.1 \frac{FV}{RT}) + 0.0365 \sigma \exp(-\frac{FV}{RT})]^{-1} \quad (4.56)$$

$$\sigma = \frac{1}{7} [\exp(\frac{[Na^+]_o}{67.3}) - 1] \quad (4.57)$$

The Na⁺ - K⁺ pump current calculated using the Runge-Kutta (4,5) integration method is shown in FIGURE 4 - 23. The result is in agreement with the result from Courtemanche et al. (Courtemanche et al. 1998).

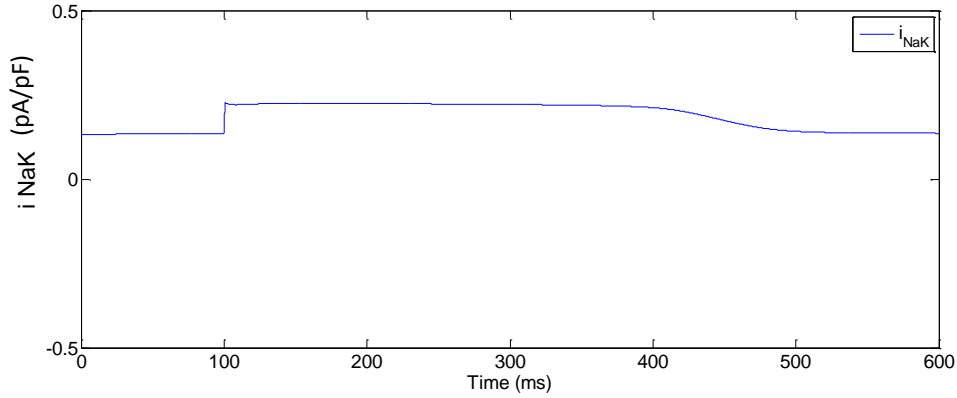


FIGURE 4 - 23 - Na⁺- K⁺ pump current in a period of 1000 ms and stimulus current at 100 ms.

4.2.10 Na⁺-Ca²⁺ Exchanger Current

This current is given by:

$$I_{Na,Ca} = \frac{I_{NaCa(max)} \left\{ \exp\left[\frac{\gamma FV}{RT}\right] [\gamma Na^+]_i^3 [Ca^{2+}]_o - \exp\left[\frac{(\gamma-1)\gamma FV}{RT}\right] [Na^+]_o^3 [Ca^{2+}]_i \right\}}{(K_{m,Na}^3 + [Na^+]_o^3)(K_{m,Ca} + [Ca^{2+}]_o) \cdot \{1 + K_{sat} \exp\left[\frac{(\gamma-1)FV}{RT}\right]\}} \quad (4.58)$$

where $I_{NaCa(max)} = 1600.0$, $\gamma = 0.35$, $K_{m,Na}$ and $K_{m,Ca}$ are the $[Na^+]_i$ and $[Ca^{2+}]_o$ half saturation constants, respectively, and $K_{sat} = 0.1$ is a saturation factor (Courtemanche et al. 1998).

The Na⁺- Ca²⁺ exchanger current calculated using the Runge-Kutta (4,5) integration method is shown in FIGURE 4 - 24.

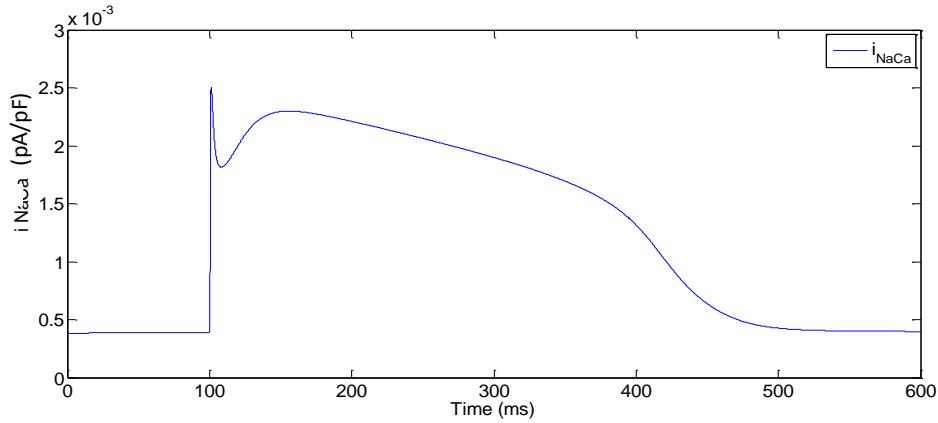


FIGURE 4 - 24 - Na^+ - Ca^{2+} exchanger current in a period of 1000 ms and stimulus current at 100 ms.

4.2.11 Background Na^+ Current

The background Na^+ current is given by:

$$I_{b,Na} = g_{b,Na}(V - E_{Na}) \quad (4.59)$$

where $g_{b,Na}$ is the maximal conductance for Na^+ (Courtemanche et al. 1998).

FIGURE 4 - 25 shows the background Na^+ current calculated using the Runge-Kutta (4,5) integration method.

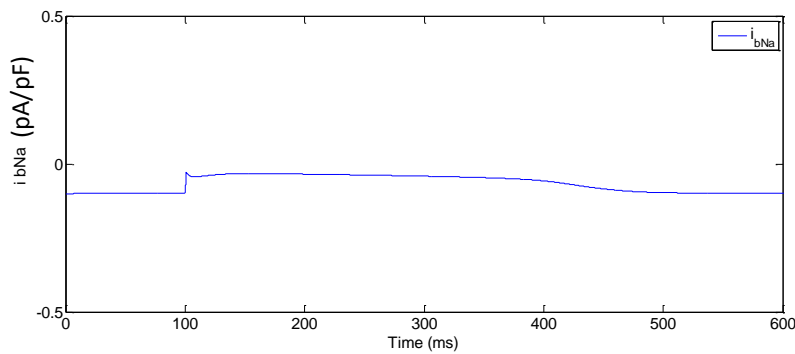


FIGURE 4 - 25 - Background Na^+ current in a period of 1000 ms and stimulus current at 100 ms.

4.2.12 Background Ca²⁺ Current

This current is given by:

$$I_{b,ca} = g_{b,ca}(V - E_{Ca}) \quad (4.60)$$

where $g_{b,ca}$ is the maximal conductance for Ca²⁺ (Courtemanche et al. 1998).

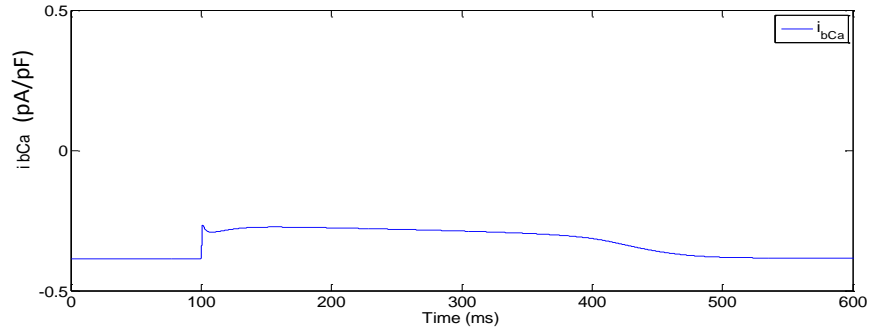


FIGURE 4 - 26 - Background Ca²⁺ current in a period of 1000 ms and stimulus current at 100 ms.

4.2.13 Ca²⁺ Uptake Current into NSR

This current is given by:

$$I_{up} = \frac{I_{up(max)}}{1 + \left(\frac{K_{up}}{[Ca^{2+}]_i}\right)} \quad (4.61)$$

where $I_{up(max)}$ is the maximal Ca²⁺ uptake rate and K_{up} is the $[Ca^{2+}]_i$ half saturation constant (Courtemanche et al. 1998).

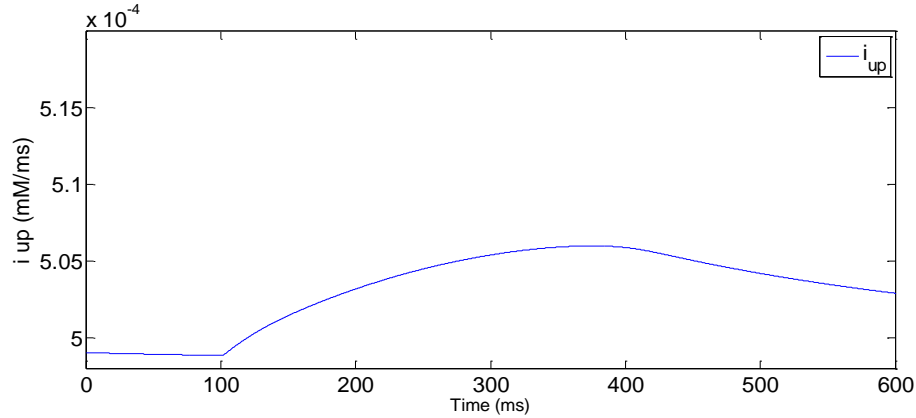


FIGURE 4 - 27 - Ca²⁺ uptake current into NSR current in a period of 1000 ms and stimulus current at 100 ms.

4.2.14 Ca²⁺ Leak Current from NSR

Ca²⁺ leak current from NSR is given by:

$$I_{up,leak} = \frac{[Ca^{2+}]_{up}}{[Ca^{2+}]_{up,max}} I_{up,max} \quad (4.62)$$

where $[Ca^{2+}]_{up,max}$ is the maximal Ca²⁺ concentration in NSR (Courtemanche et al. 1998).

Ca²⁺ leak current from NSR with the Runge-Kutta (4,5) integration method is shown in FIGURE 4 - 28.

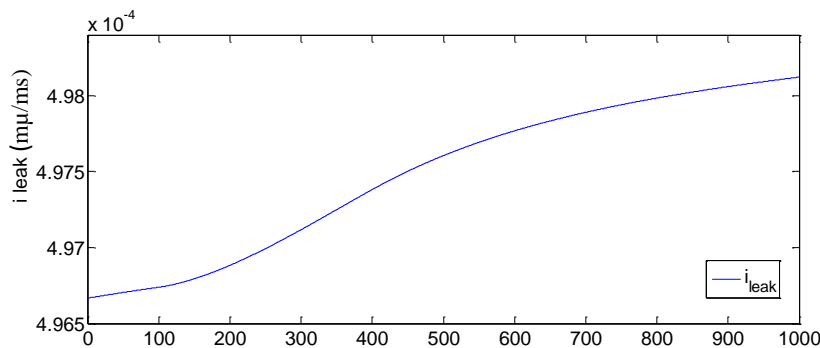


FIGURE 4 - 28 - Ca²⁺ leak current from NSR current in a period of 1000 ms and stimulus current at 100 ms.

4.2.15 Ca²⁺ Release Current from JSR

Ca²⁺ release current from JSR is given by:

$$I_{rel} = K_{rel}u^2vw([Ca^{2+}]_{rel} - [Ca^{2+}]_i) \quad (4.63)$$

where K_{rel} is the maximal release rate for I_{rel} , u , v , and w are gating variable (Courtemanche et al. 1998), which satisfy equation (4.48) with the following coefficients:

$$\tau_u = 8.0, \quad u_\infty = \left(1 + \exp\left[-\frac{F_n - 3.4175 \times 10^{-13}}{13.67 \times 10^{-16}}\right]\right)^{-1} \quad (4.64)$$

$$\tau_v = 1.91 + 2.09 \left(1 + \exp\left[-\frac{F_n - 3.4175 \times 10^{-13}}{13.67 \times 10^{-16}}\right]\right)^{-1} \quad (4.65)$$

$$V_\infty = 1 - \left(1 + \exp\left[-\frac{F_n - 6.835 \times 10^{-14}}{13.67 \times 10^{-16}}\right]\right)^{-1} \quad (4.66)$$

$$\tau_w = 6.0 \frac{1 - \exp\left(-\frac{V-7.9}{5}\right)}{\left[1 + 0.3 \exp\left(-\frac{V-7.9}{5}\right)\right]^{(V-7.9)}} \quad (4.67)$$

$$W_\infty = 1 - \left[1 + \exp\left(-\frac{V-40}{17}\right)\right]^{-1} \quad (4.68)$$

$$F_n = 10^{-12}V_{rel}I_{rel} - \frac{5 \times 10^{-13}}{F} \left(\frac{1}{2}I_{Ca,L} - \frac{1}{5}I_{NaCa}\right) \quad (4.69)$$

where F_n is the sarcoplasmic Ca²⁺ flux signal (Courtemanche et al. 1998).

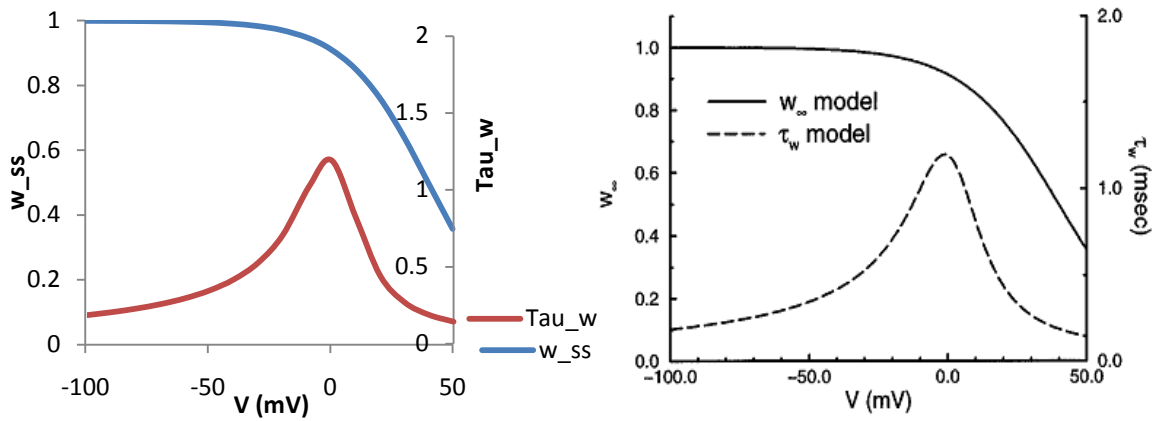


FIGURE 4 - 29 - Steady state activation and inactivation curves of the Ca^{2+} release current from JSR parameters. The data given in the Courtemanche et al. report is shown on the left figure (Courtemanche et al. 1998).

FIGURE 4 - 30 shows the gating parameters of the Ca^{2+} release current from JSR generated with the Runge-Kutta (4,5) integration method. The result is in agreement with data from Courtemanche et al.

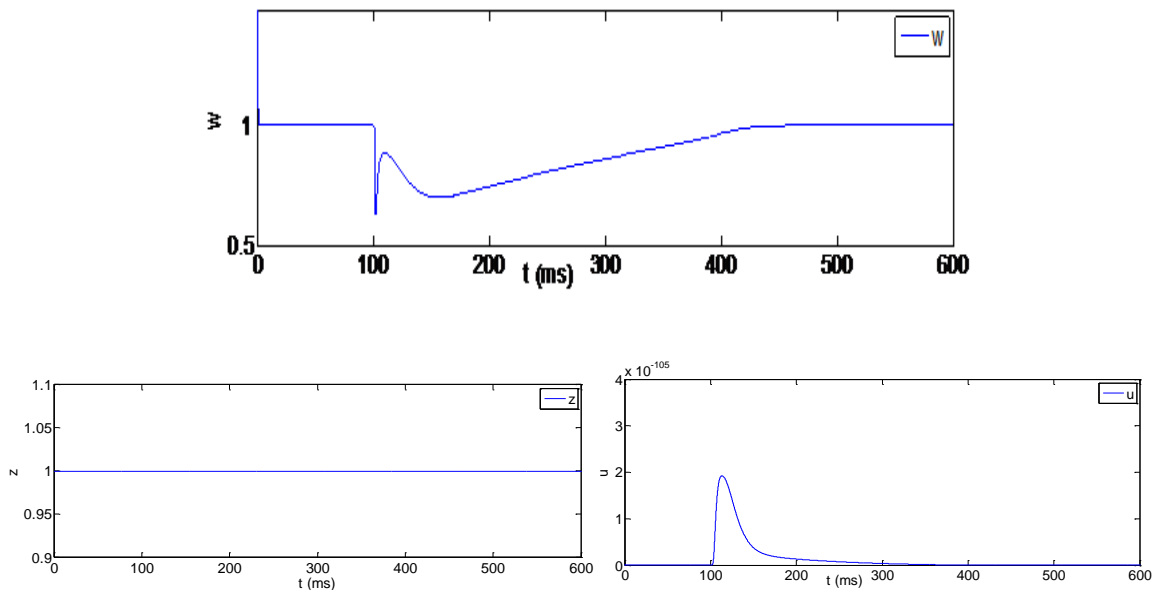


FIGURE 4 - 30 - Gating parameter variables of the Ca^{2+} release current from JSR at a period of 1000 ms.

I_{rel} has a very small value and is slightly changed during action potential duration.

I_{rel} current is shown in FIGURE 4 - 31.

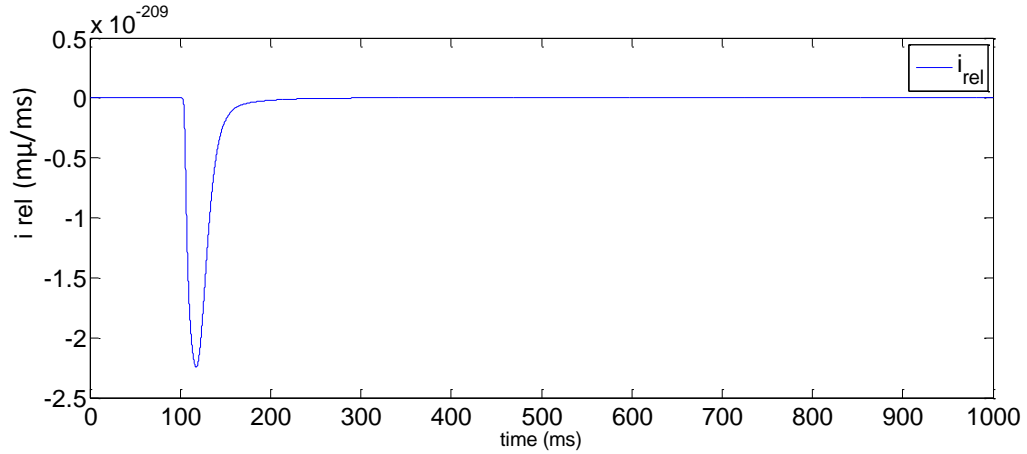


FIGURE 4 - 31 - Ca^{2+} release current from JSR current in a period of 1000 ms and stimulus current at 100 ms.

4.2.16 Ca^{2+} Transfer Current from NSR to JSR

Finally, the calcium transfer current from NSR to JSR is given by:

$$I_{tr} = \frac{[Ca^{2+}]_{up} - [Ca^{2+}]_{rel}}{\tau_{tr}} \quad (3.70)$$

where $\tau_{tr} = 180$ (Courtemanche et al. 1998).

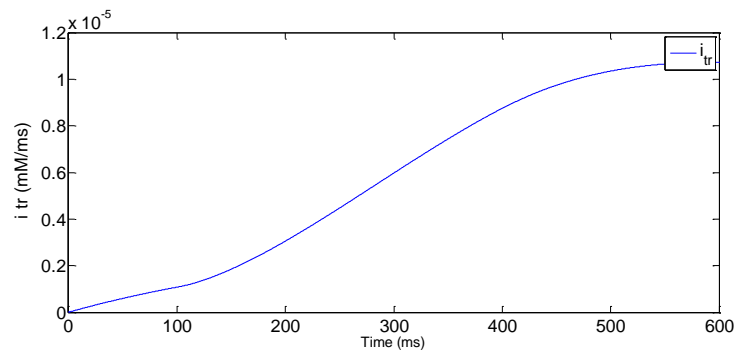


FIGURE 4 - 32 - Ca^{2+} current from NSR to JSR in a period of 1000 ms and stimulus current at 100 ms.

4.2.17 Total Ionic Current

Total ionic current is given as follows and is shown in FIGURE 4 - 33.

$$I_{ion} = I_{Na} + I_{K1} + I_{to} + I_{Kur} + I_{Kr} + I_{Ks} + I_{Ca,L} + I_{p,Ca} + I_{NaK} + I_{NaCa} + I_{b,Na} + I_{b,Ca}$$

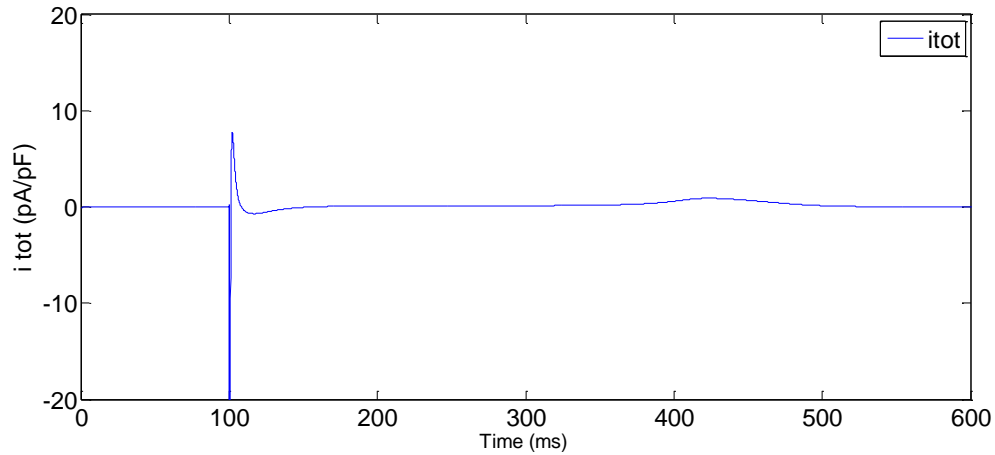


FIGURE 4 - 33 - Total current in a period of 1000 ms and stimulus current at 100 ms.

Twelve ionic currents are involved in this model. FIGURE 4 - 34 shows the role of these currents during the action potential.

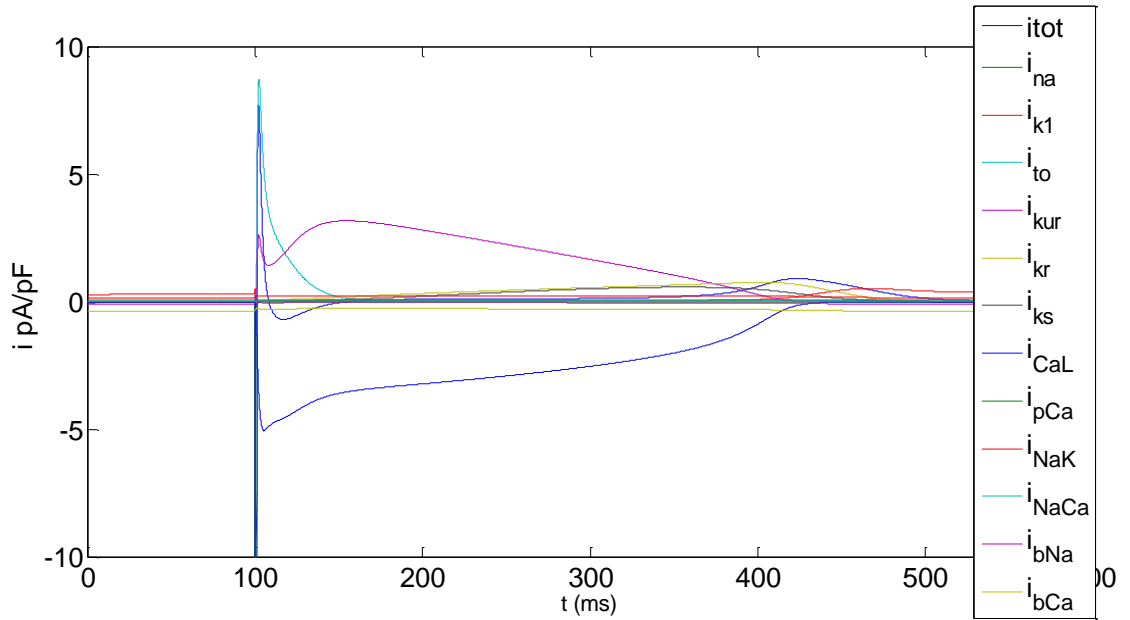


FIGURE 4 - 34 - 12 ionic currents in a period of 1000 ms and stimulus current at 100 ms solved with the Runge-Kutta (4,5) integration method.

As FIGURE 4 - 34 shows, the L-type Ca^{2+} current i_{CaL} and the outward K^+ currents i_{to} , i_{kr} , and i_{kur} have the most significant role in the atrial cell action potential. However, the significance of the other ionic currents is still important for accurate modeling.

4.2.18 Atrial Cell Action Potential

Action potential of an atrial cell is generated using the Courtemanche et al. model and solving a system of ODEs using Matlab ode solver Equation (4.71).

$$\frac{dV}{dt} = \frac{-(I_{\text{ion}} + I_{\text{st}})}{C_m} \quad (4.71)$$

FIGURE 4 - 35 shows the atrial cell membrane action potential generated with the Runge-Kutta (4,5) integration method. The result is in agreement with the result from Courtemanche, et al.

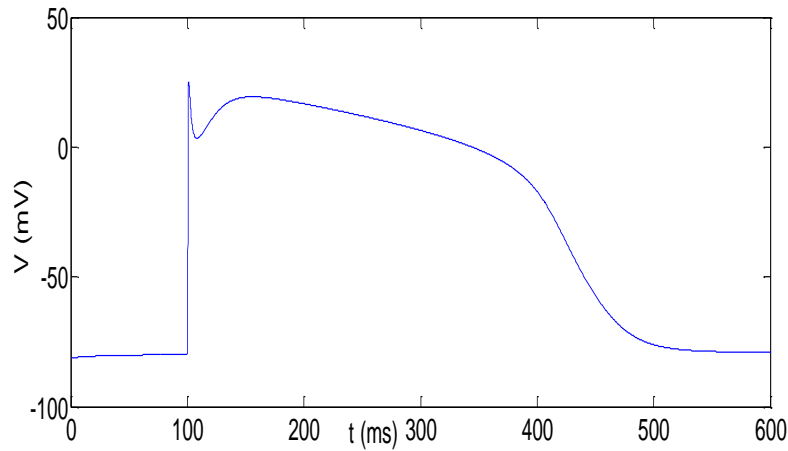


FIGURE 4 - 35 - Atrial cell membrane action potential.

The action potential duration can be shortened for faster rates by altering the channel conductance of L-type Ca^{2+} current i_{CaL} , the outward K^{+} currents i_{to} , i_{kr} , and i_{kur} (Courtemanche et al. 1998).

FIGURE 4 - 36 shows faster rate in APD by altering i_{CaL} , i_{to} , i_{kr} , and i_{kur} by factors 1.2, 0.3, 0.7, and 1.2 respectively (A) and 1.6, 0.15, 0.5, 1.2 respectively (B).

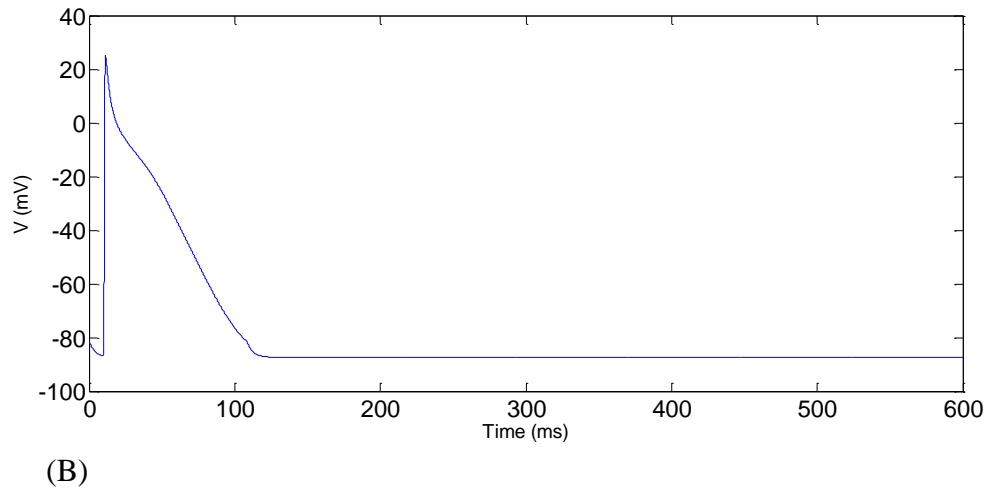
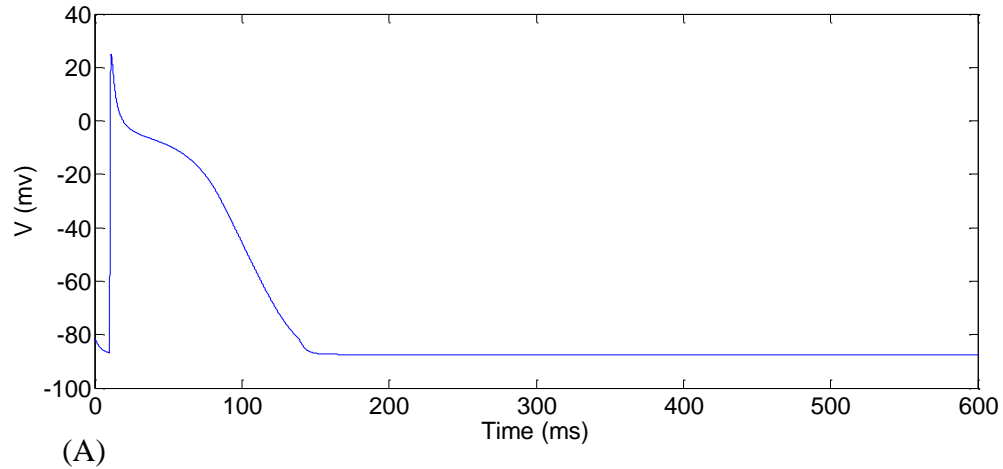


FIGURE 4 - 36 - Altered membrane action potential for a faster rate. i_{CaL} , i_{to} , i_{kr} , and i_{kur} are altered by factors 1.2, 0.3, 0.7, and 1.2 respectively (A) and 1.6, 0.15, 0.5, 1.2 respectively (B).

4.3 Atrial Tissue Model

A two-dimensional model of human atrial tissue was developed using an ionic-based membrane model. A small section of atrial tissue was constructed with one type of cell. The cells making up the tissue were assumed to be identical and connected to each other in a uniform way. The tissue was assumed to be isotropic; hence the conductivity

tensors were set to a same value in two directions. There are no currents flowing into and out of the tissue.

Cardiac cells are connected to one another via gap junctions. The electrical propagation of the cardiac impulse is obtained by solving a reaction diffusion system based on the ionic model. The propagation of action potential is modeled assuming monodomain equation given by: (Henriquez & Papazoglou, 1996)

$$C_m \frac{\partial V_m}{\partial t} = S_v^{-1} \nabla \cdot \sigma \nabla V_m + I_{st} - I_{ion} \quad (4.80)$$

where V_m is the transmembrane voltage (mV), $C_m = 1(\mu\text{F}/\text{cm}^2)$ represents the membrane capacitance, $S_v = 0.24(\mu\text{m}^{-1})$ the cell surface to volume ratio, $\sigma = 0.5$ (mS/m) the electrical conductivity tensor of atrial tissue, I_{st} is the external stimulus current density to generate action potential and I_{ion} is the total ionic current calculated using the Courtemanche et al. cell model (Courtemanche et al. 1998).

The stimulus current is applied in a small region of the tissue and action potential propagation is modeled. FIGURE 4 - 37 shows the schematic of the model.

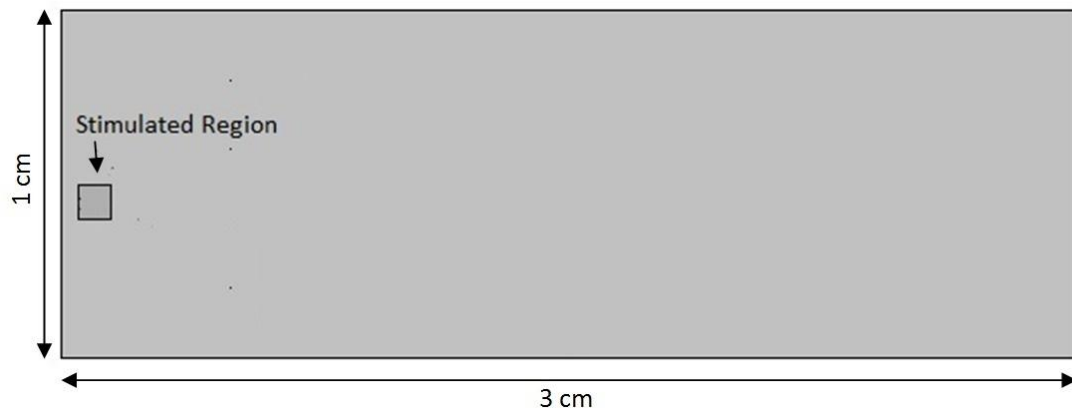


FIGURE 4 - 37 - Two-dimensional atrial tissue model.

Electrical propagation in atrial tissue involves both the intracellular and extracellular compartments (bidomain model) (Skouibine et al. 2000). According to Poste, et al. the difference between monodomain and bidomain results is very small (Potse et al. 2006). Therefore, the monodomain model is used in this project due to the lower computational demand.

COMSOL Multiphysics is used as the finite element modeling tool in this research to model the propagation of action potential in a two-dimensional rectangular slice of atrial tissue.

In COMSOL Multiphysics 4.1 the PDE in coefficient form is taken:

$$e_a \frac{\partial^2 V}{\partial t^2} + d_a \frac{\partial V}{\partial t} + \nabla(-c\nabla V - \alpha V + \gamma) + \alpha V + \beta \nabla V = f \quad (4.81)$$

For implementing Equ.4.80 in Equ.4.81, the variables are replaced with appropriate expressions.

The ionic current is taken from the cell model. The ionic current is a function of transmembrane potential, gating and ion concentration. Each gating parameters described in the cell model is implemented in the COMSOL using the PDE in the coefficient form. For each point, a system of 21 coupled nonlinear differential equations is solved. For the two-dimensional tissue simulation we considered a 3 X 1 cm rectangle. The computational model has 2700 nodes, where each node was assumed to contain a group of cells that all behave the same. A rectangular stimulus impulse was applied to the electrode and the action potential propagation is calculated in the domain. FIGURE 4 - 38 shows the membrane action potential as a function of time at 4 different locations. It clearly shows the excitation of the tissue as a response to a single stimulation impulse

applied to the electrode on the right side. The propagation of action potentials and their moving direction in 2D tissue is shown in FIGURE 4 - 39.

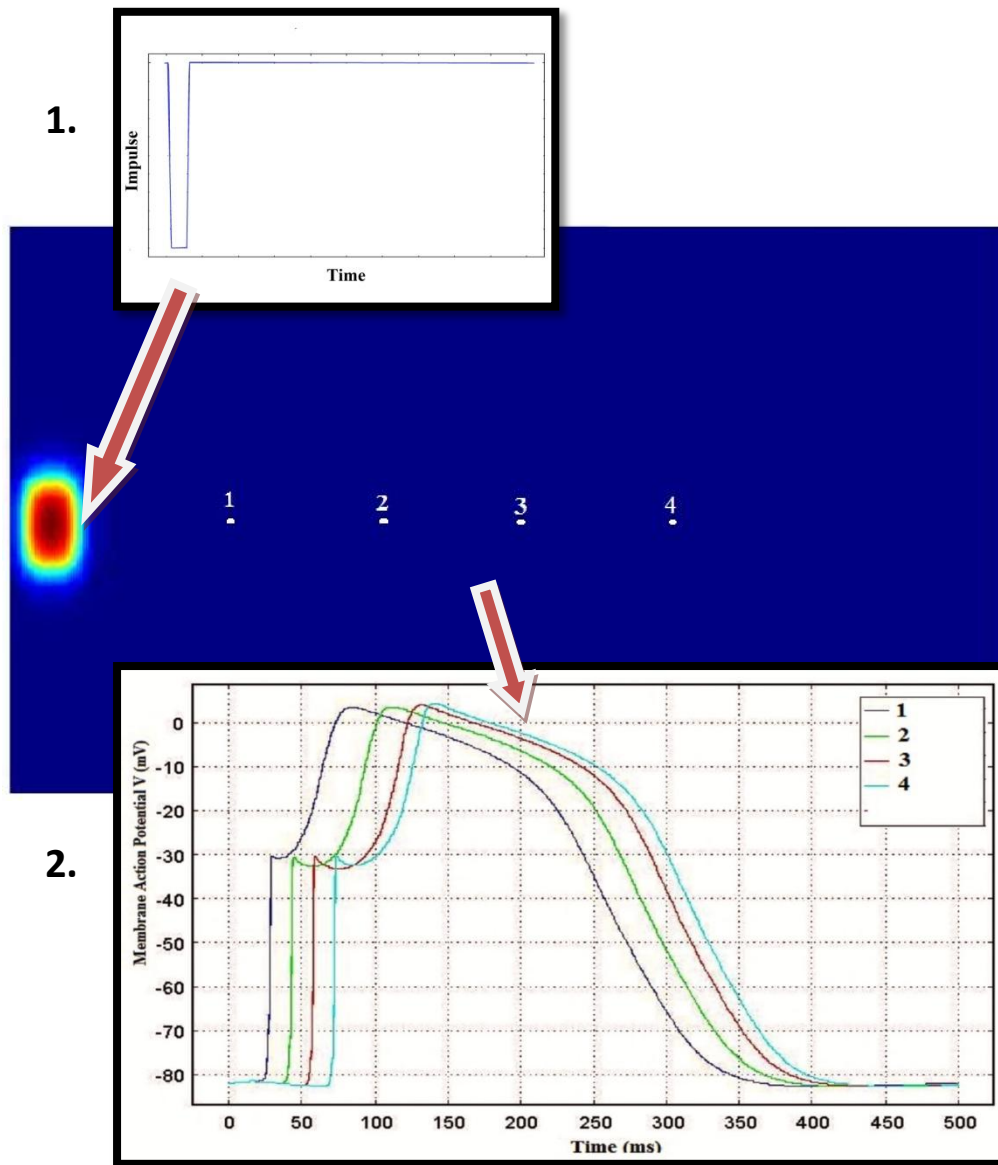


FIGURE 4 - 38 - Membrane action potential V as a function of time at 4 different locations. A rectangular stimulation impulse is applied to the electrode on the right side of the tissue (1). Action potential propagation in the tissue (2).

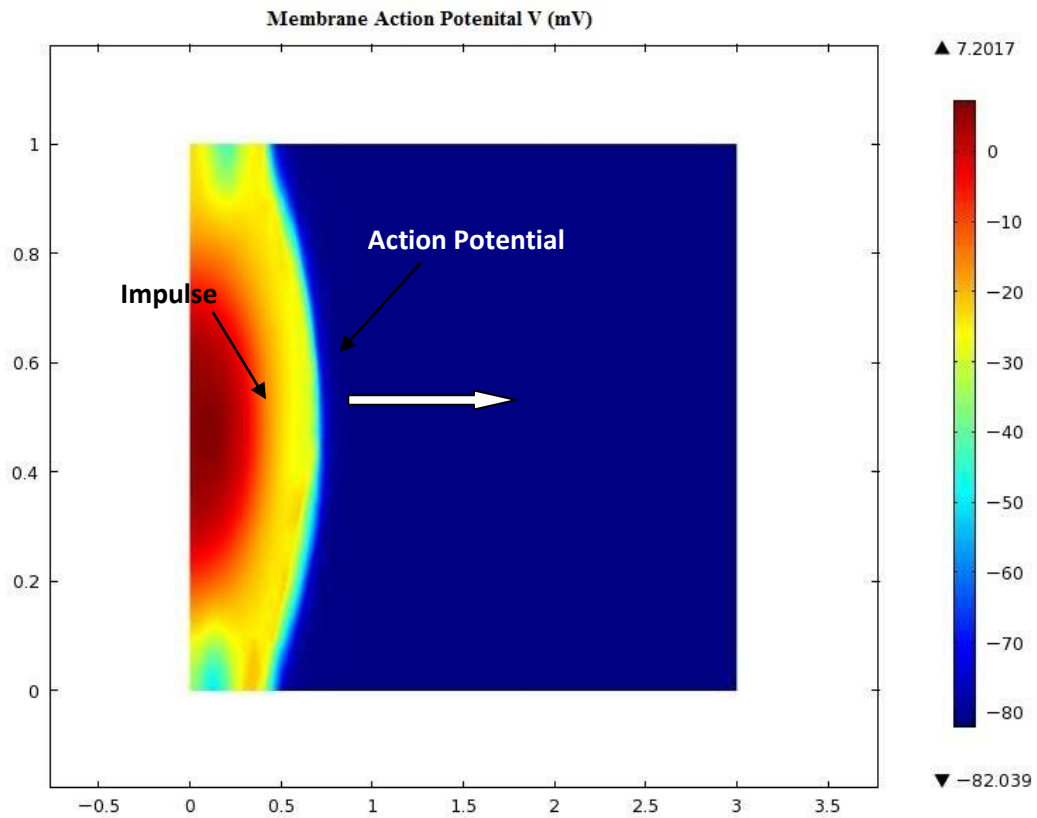


FIGURE 4 - 39 - Two-dimensional propagation of atrial action potential. A rectangular 5 ms impulse is applied at the right side. The resulting action potential propagation is shown at time = 20 ms. The arrow shows the direction of action potential propagation.

CHAPTER 5

ATRIAL ELECTROGRAM MODEL

5.1 Introduction

Atrial electrograms are recorded during mapping studies in patients with AF. The electrogram is the recording of the extracellular potential.

The extracellular potential Φ_e was modeled based on the current source approximation for a large unbounded volume conductor (Lesh et al. 1988).

$$\Phi_e(x, y, t) = \frac{1}{4\pi\sigma_e} \sum \frac{I_m}{|r|} \quad (5.1)$$

where σ_e is the extracellular conductivity (the saline bath conductivity) 1.5 (S/m), $|r|$ is the distance between the recording electrode and the tissue, and I_m is the transmembrane current ($\mu\text{A}/\text{cm}^3$) given by:

$$I_m = \nabla \cdot \sigma \nabla v \quad (5.2)$$

The extracellular potential calculated above gives a unipolar recording. The bipolar recording is the difference between the two unipolar electrograms (Podrid & Kowey, 2001).

5.2 Electrogram Model

The stimulus current was applied in a small region of the tissue and an electrode array recorded the extracellular potential on the tissue. The electrode array dimensions were based on the electrode catheter used to record human atrial electrograms. FIGURE 5 - 1 shows the schematic of the tissue model and dimensions of the electrode catheter.

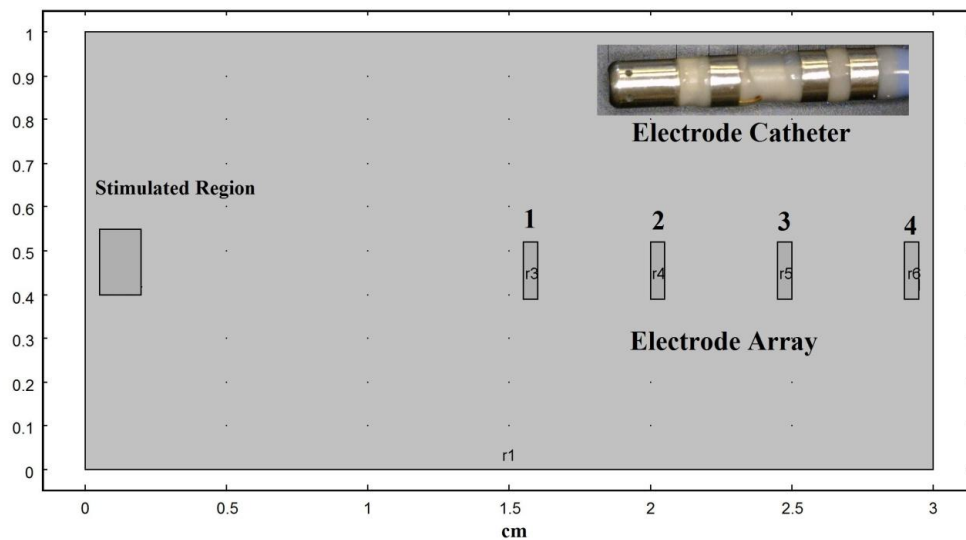


FIGURE 5 - 1 - Two-dimensional atrial tissue with an electrode array and a stimulus region. Electrode catheter used to record human atrial electrograms is shown on the top right corner.

The unipolar electrograms were modeled relative to the zero reference potential in an unbounded bath. FIGURE 5 - 3 represents the comparison of the unipolar recording computed by the model at 4 locations using unipolar electrodes and a human unipolar electrogram. It shows that the electrogram model is similar to the atrial electrogram obtained from the patient.

The electrogram obtained from the patient was the high right atrium electrograms (HRA) (FIGURE 5 - 2) including both atrial and ventricular electrical activities. The signals related to the atrial were extracted to be compared to the model.

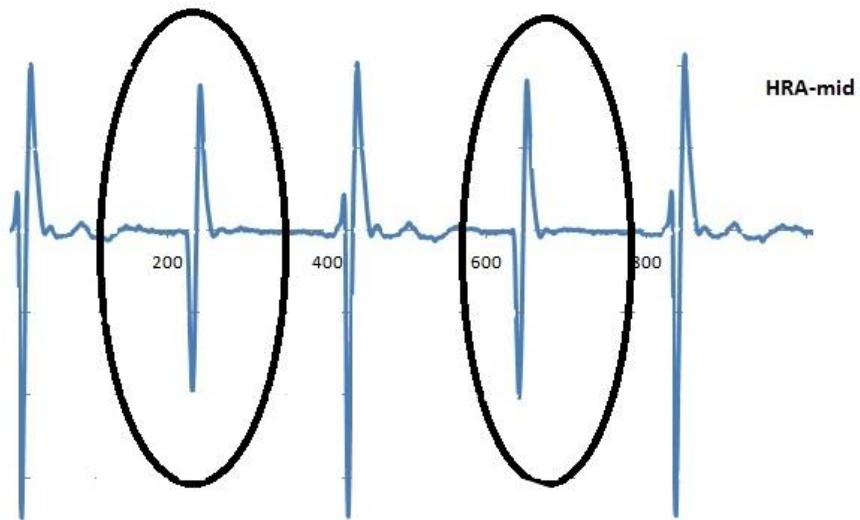


FIGURE 5 - 2 - High right atrium electrogram obtained from a patient. The atrial electrograms are marked.

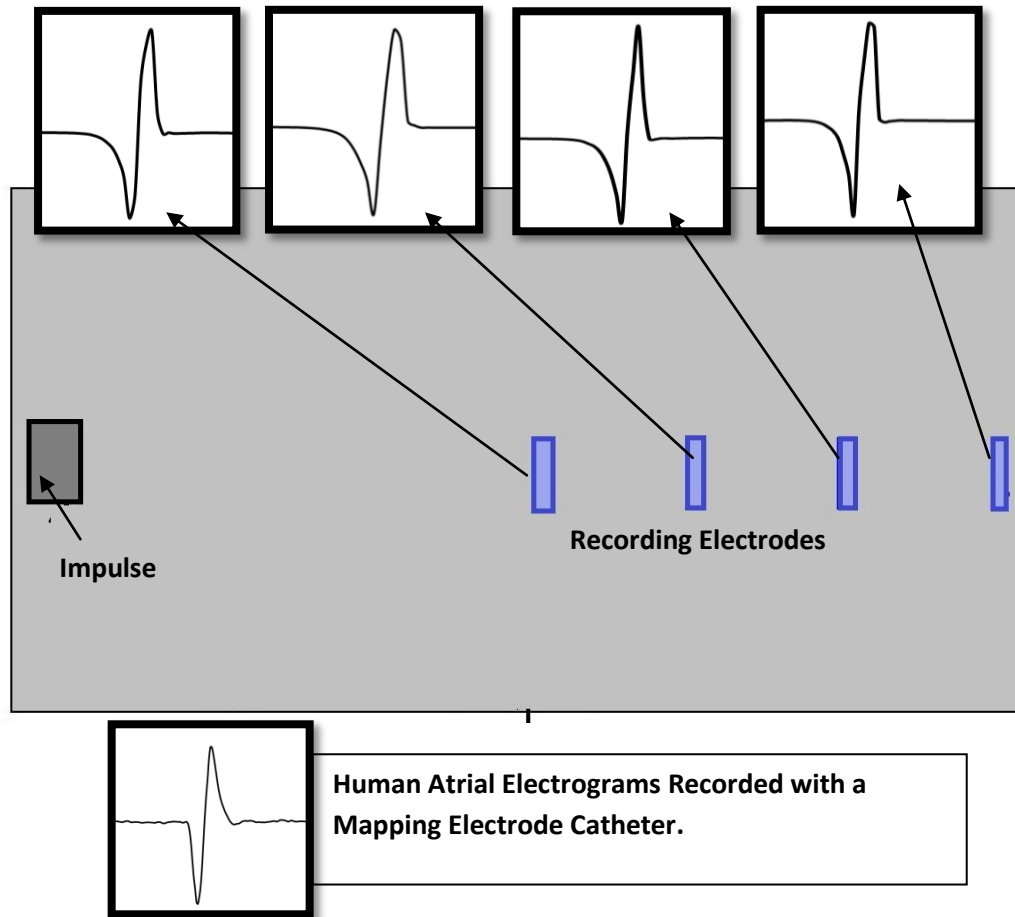


FIGURE 5 - 3 - Atrial electrograms were computed at 4 locations on unipolar electrodes. The computed atrial electrograms are in agreement with the human atrial electrograms recorded with a mapping electrode catheter.

The size of the electrode is a significant factor in reducing the background noise during the electrogram recording. Therefore, the smaller the surface area of the plates is, the less background noise will capture (FIGURE 5 - 4). The electrograms shown in FIGURE 5 - 4 are computed from electrode 1 with the similar conditions.

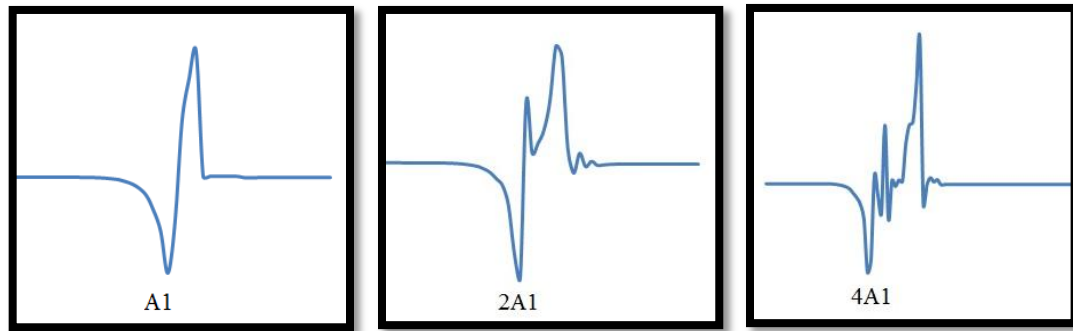


FIGURE 5 - 4 - The background noise increases by increasing the electrode surface area by factors of 2 and 4.

Another important factor in electrograms recording using electrode array is the distance between the recording electrodes and the tissue. The distance is proportional to the amplitude size of the signal. An increase in the distance of the recording electrode and the tissue decreases the amplitude of the signal. Typical distance during mapping procedure is approximately 5mm. FIGURE 5 - 5 represents that increasing the distance between the recording electrode and tissue decreases the amplitude of the signal.

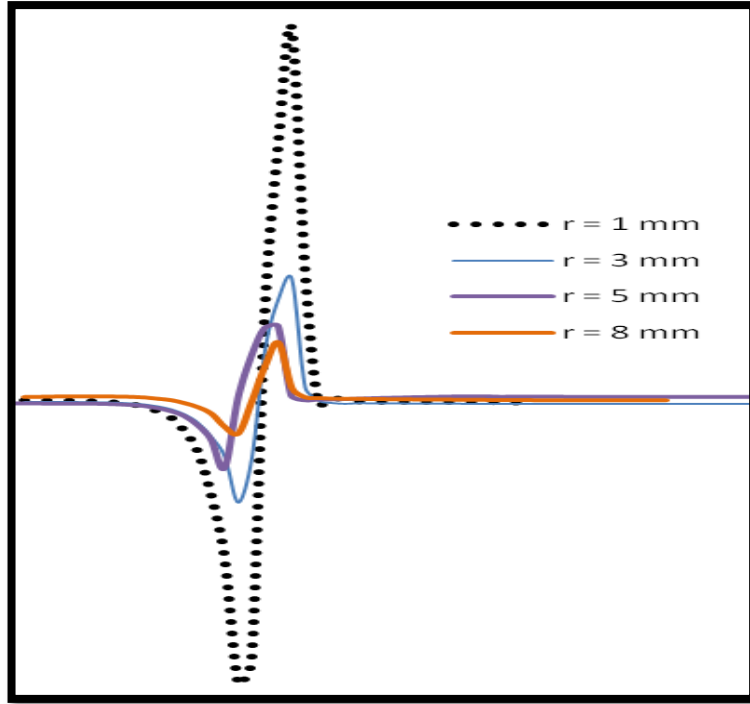


FIGURE 5 - 5 - Unipolar electrogram computed in 4 different distances at the same location. It shows that the amplitude of the signal decreases as the distance gets increased.

Bipolar atrial electrograms are more distinct and recorded during human mapping recording (Moss & Allen, 2007). Bipolar electrogram was also modeled by taking the difference between two unipolar electrograms (Podrid & Kowey, 2001). FIGURE 5 - 6 shows the bipolar electrogram computed based on the electrodes 1 and 2. It clearly shows that the bipolar electrogram model is identical to the bipolar electrogram obtained from the patient.

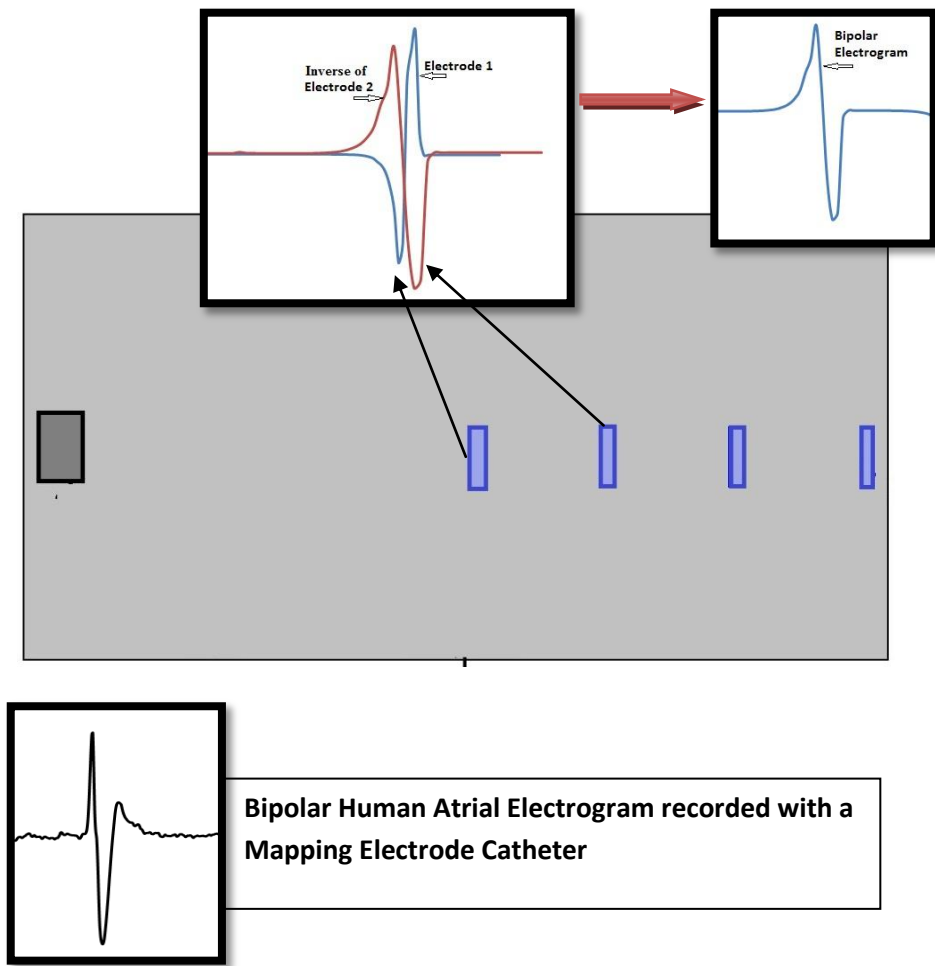


FIGURE 5 - 6 - Bipolar electrogram obtained from the difference between the electrograms recorded at two unipolar electrodes. The computed bipolar electrogram is in agreement with the bipolar human atrial electrogram recorded with a mapping electrode catheter.

CHAPTER 6

ATRIAL FIBRILLATION ABLATION MODEL

6.1 Introduction

The final goal of the project is to understand the effect of ablation lines in the electrical propagation in the atrium. Fibrillation can be induced to the model by applying rapid stimulation. Then, simulating an ablation line with a computer model is simple and was done by defining an additional domain located between the stimulated region and electrode array with lower electrical conductivity. Two electrodes recorded the electrograms at two sides of the ablation line.

The primary goal of creating ablation lines in the atria is to create insulated barriers in the tissue to redirect the disorganized signals to follow a normal pathway. It is very important to create a continuous and transmural ablation lines. Any discontinuities in the ablation line can lead to the reentries and sustaining the fibrillation.

Creating linear scars in the tissue destroys some excitable cells and alters the conductivity properties of the tissue. Ablated areas are replaced by fibrous tissues during healing (Haines, 2000). The conductivity of fibrous tissue is less than normal myocardial tissue.

Atrial fibrillation ablation therapy was modeled by simulating an ablation line located in the two-dimensional tissue model, giving rise to an additional domain located

between the stimulated region and electrode array (FIGURE 6 - 1). The behavior of the electrical propagation is investigated with a complete ablation and a fractional ablation.

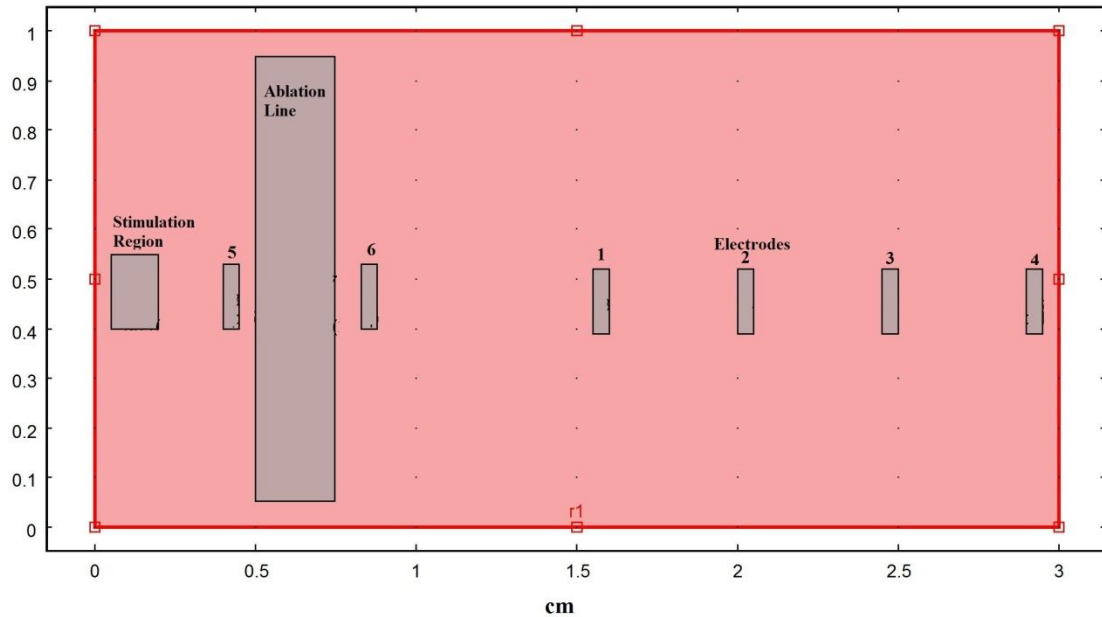


FIGURE 6 - 1 - Two-dimensional atrial tissue with a fractional ablation line.

As it was mentioned, the ablation region has a lower conductivity than the rest of the myocardial tissue. However, the change in conductivity does not occur at the time of ablation. Conductivity change happens after the healing process is complete. Healing time for ablation therapy is normally long and could be about six to eight weeks (Elsaie & Choudhary, 2010). However, when the scars form, fibrous tissue replaces the normal myocardial tissue. This will result in the change of the electrical conductivity of the area. The fibrous tissue has a very large resistivity; therefore, the electrical conductivity of the ablation line is assumed to be very close to zero (0.05 mS/m). We also studied the behavior of the model as the conductivity of the ablation line decreases from normal conductivity (0.5 S/m) to zero.

6.2 Complete Ablation

Complete ablation prevents the propagation of action potential. FIGURE 6 - 2 shows the action potential behavior and the electrograms computed at both sides of the complete ablation line. If the ablated tissue is completely replaced by fibrous tissue, the electrical conductivity of the lesion will be close to zero. Therefore, it does not propagate the action potential. As a result, the action potential will not reach the other side of the ablation line.

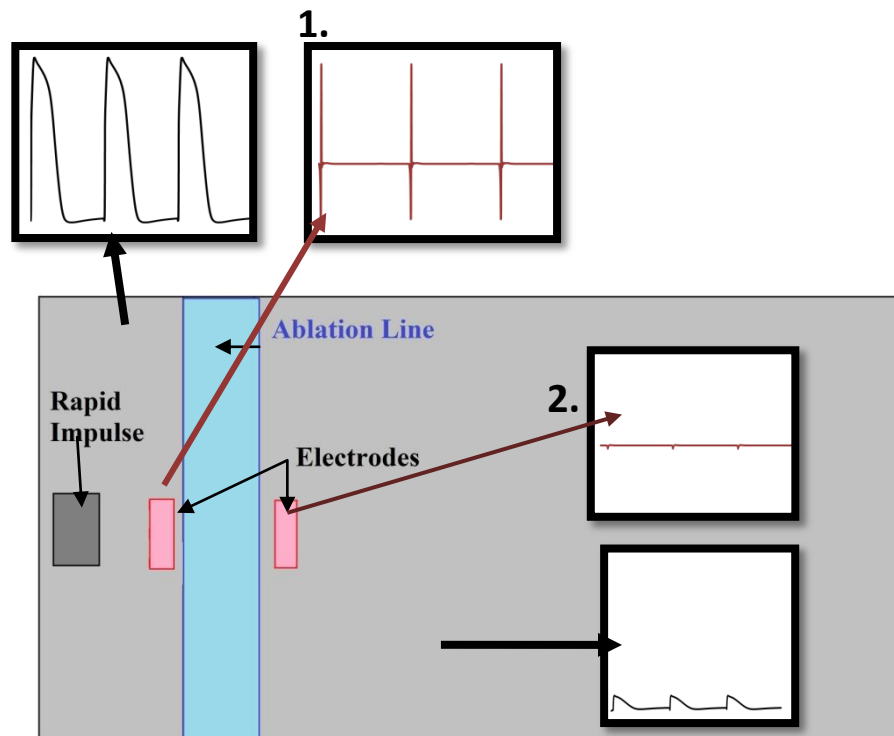


FIGURE 6 - 2 - Fibrillation induced to the model including a complete ablation line by rapid stimulation. A complete ablation line with electrical conductivity of 0.05 mS/m prevents the propagation of action. (1) Electrogram computed behind the ablation line. It shows the fibrillation as a result of rapid stimulation. (2) Electrogram computed in front of the ablation line. It shows that a complete ablation line with electrical conductivity of 0.05 mS/m prevents the propagation of action potential.

FIGURE 6 - 3 shows the propagation of action potential in the two-dimensional tissue model. The currents cannot fully flow through the ablation line and reach the other side of the tissue.

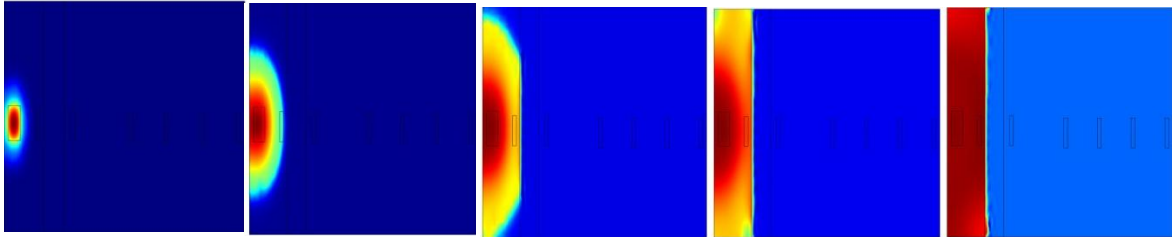


FIGURE 6 - 3 - Two-dimensional propagation of action potential in a tissue with a complete ablation line.

6.3 Fractional Ablation

Fractional ablation allows the propagation of action potential through the gaps. It causes action potential delay. The currents flow through the gaps and reach the other side of the ablation line. FIGURE 6 - 4 shows the action potentials and the electrograms computed at both sides of a fractional ablation line. The figure shows that the action potential reaches the other side of the ablated line with some time delay.

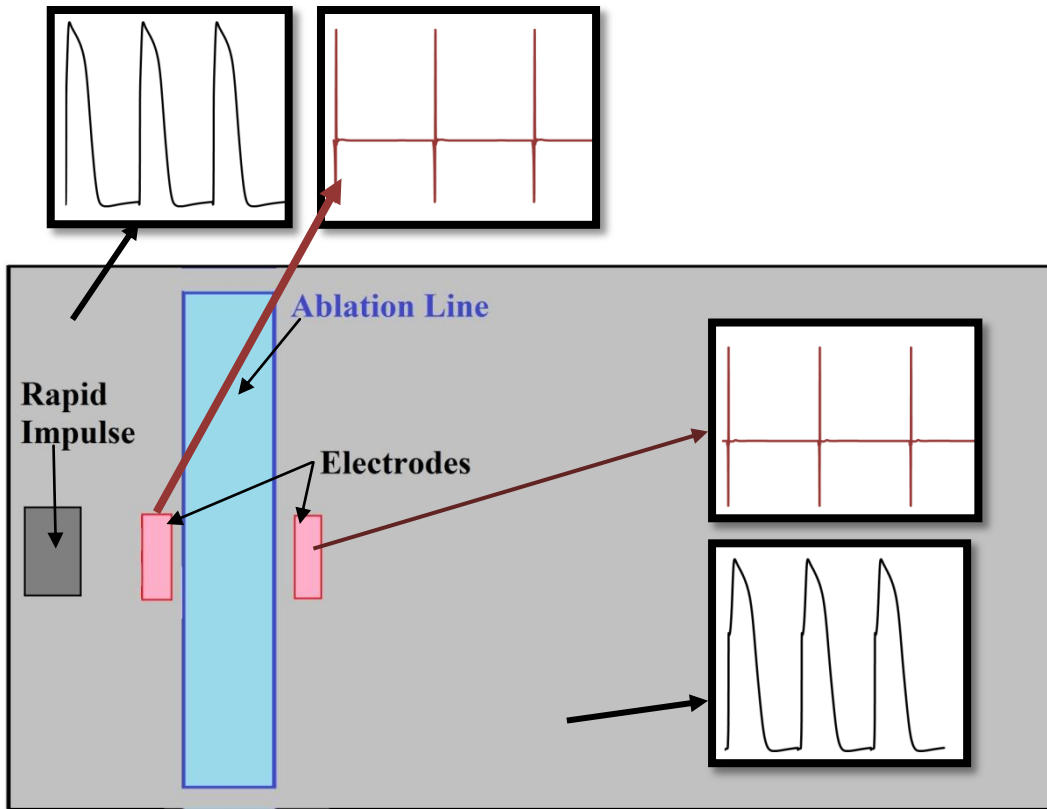


FIGURE 6 - 4 - Fibrillation induced to the model including a fractional ablation line by rapid stimulation. A fractional ablation line with electrical conductivity of 0.05 mS/m was applied to the model. Action potentials propagate through the gaps and activate the tissue on the other side of the ablation line. (1) Electrogram computed behind the ablation line. It shows the fibrillation as a result of rapid stimulation. (2) Electrogram computed in the front of the ablation line. It shows the similar behavior on the other side of the ablation line with some excitation delay.

The membrane potential propagation in the two-dimensional tissue is shown in FIGURE 6 - 5. The figure shows how the action potential propagates through the gaps and reaches the other side of the ablation line.

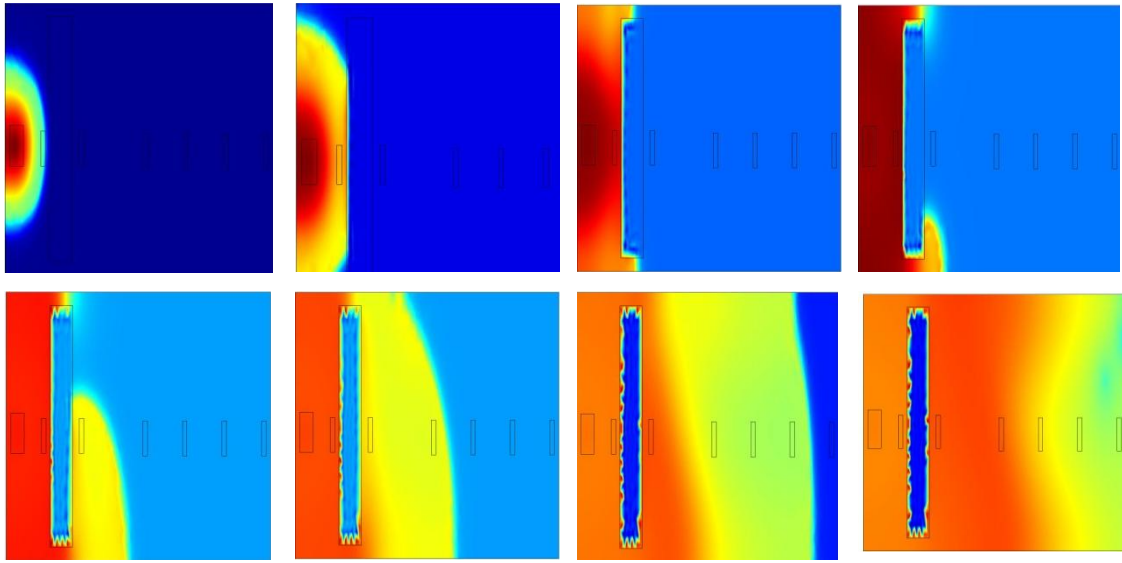


FIGURE 6 - 5 - Two-dimensional propagation of action potential in a tissue with a fractional ablation line.

6.4 The Effect of Change Conductivity

In the last section of this chapter, we studied the effect of change in the lesion electrical conductivity on the propagation of action potential. The speed of action potential propagation decreases by decreasing the conductivity of the ablation line. FIGURE 6 - 6 shows the electrograms computed at the first electrode of the electrode array on the tissue including a complete ablation line. The stimulus impulse is applied at 1ms. The electrical conductivity of the ablation line is set to be 0, 0.05, 0.1, and 0.5 (mS/m). Decreasing the conductivity of the ablation line delays the excitation of the tissue at the locations behind the ablation line. Complete ablation lines with electrical conductivity close to zero prevent the propagation of action potential.

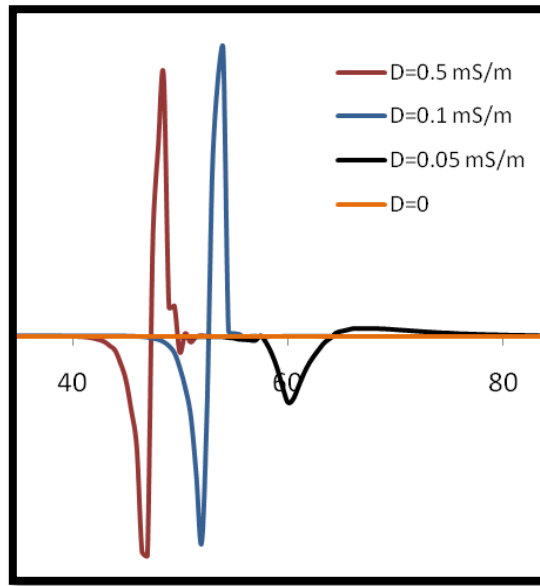


FIGURE 6 - 6 - Atrial electrograms computed at the electrode 1 on tissue with a complete ablation line with electrical conductivities of 0.5, 0.1, 0.5, and 0 mS/m.

CHAPTER 7

CONCLUSIONS AND FUTURE WORK

The purpose of this thesis has been the construction of a two-dimensional atrial tissue model to study the propagation of action potential and electrograms. The key points of the project are summarized here and followed by a review of possible future directions.

7.1 Conclusions

The impact of atrial fibrillation in terms of prevalence and challenging treatment has been underlined. The emergence of computer models and mathematical simulations in this field with their advantages has been provided.

A brief overview of the overall function of the human cardiovascular system and atrial fibrillation has been presented. It has been discussed the main aspects of atrial fibrillation. Overviews of the currently available ablation procedure for atrial fibrillation treatment and its limitations have been discussed.

The electrical activity of the heart and the concepts of cell excitability and action potential have been described. A description of the principal ions involved in the action potential has been provided. The standard mathematical model of cardiac action potential has been presented in this chapter as well.

The Courtemanche et al. atrial cell model has been generated using different numerical methods to solve ODE systems. A system of 21 differential equations has been solved with the Runge-Kutta (4,5) integration method. The result was in agreement with Courtemanche et al. The results have indicated that i_{CaL} , i_{to} , i_{kur} , and i_{K1} , have the most important role in the atrial action potential. Modifying the action potential can be achieved by altering these currents. The action potential duration can be shortened for faster rate by altering the channel conductance of these currents. Action potential propagation has been demonstrated for isotropic monodomain cardiac model in this chapter as well. The atrial action potential propagation in a two-dimensional model has been presented.

The mathematical model of atrial electrograms recorded with mapping catheter has been presented. The unipolar and bipolar electrograms have been constructed. The results were in agreement with the human atrial electrograms recorded at right atrial sites in a patient. The relationship between the size of the recording electrode and shape of the signal has been described. It has also been shown that the distance between the recording electrode and the tissue is inversely proportional to the amplitude of the signal.

The atrial ablation model has been constructed. Atrial fibrillation was induced to the model and the effect of ablation line on propagation of atrial fibrillation has been investigated. It has been shown that presenting some gaps along the ablated line allow the action potentials to propagate through those gaps; therefore, it causes a delay of a few milliseconds in excitation of the tissue behind the ablated line. However, complete ablation with conductivity of close to zero will prevent the excitation behind the ablation line.

Therefore, according to these achievements the success rate of ablation procedure is mainly correlated with the creation of a continuous lesion lines and also the formation of fibrous tissue. In order to prevent the propagation of action potential, the ablated regions of myocardial tissue must be fully replaced by fibrous tissue to produce insulated barriers with electrical conductivity close to zero. Therefore, it is possible to redirect the disorganized signals to follow a normal pathway.

7.2 Future Work

In order to better understand the behavior of the ablation lines and their role in action potential propagation, a three-dimensional realistic model of atrial needs to be constructed. The two-dimensional model of a myocardial sheet developed in this project can next be used to develop a three-dimensional model with more than one type of cells and introduce anisotropy. Consequently, the entire atrial tissue can be constructed including SA node with a realistic geometry. The model will be capable of being modified with the aim of obtaining a preferred action potential. Such a computer model can be beneficial prior to the ablation procedures to examine effects of ablation sites on treating atrial fibrillation.

REFERENCES

- "Atrial Fibrillation". (2001). Retrieved September 20, 2010, from Mayo Clinic: <http://www.mayoclinic.org/atrial-fibrillation/>
- "Atrial Fibrillation". (2002). Retrieved Sep 11, 2010, from <http://www.a-fib.com/Glossary.htm>
- "What Is Atrial Fibrillation?". (2009). Retrieved 2010, from National Heart, Lung, and Blood Institute: http://www.nhlbi.nih.gov/health/dci/Diseases/af/af_what.html
- Andrikopoulos, G., Tzeis, S., Maniadakis, N., Mavrakis, H. R., & Vardas, P. E. (2009). Cost-Effectiveness of Atrial Fibrillation Catheter Ablation. Oxford University Press, 11 (2), 147-151.
- Benjamin, E. J. (1994). Independent Risk Factors for Atrial Fibrillation in a Population-Based Cohort. The Framingham Heart Study. *JAMA*, 271(11):840-844.
- Boyle, N. G., Fleming, P., & Hale, K. L. (2011). Atrial Fibrillation. Retrieved 15 2011, 02, from [emedicinehealth: http://www.emedicinehealth.com/atrial_fibrillation/article_em.htm](http://www.emedicinehealth.com/atrial_fibrillation/article_em.htm)
- Cherry, E., Greenside, H., & Henriquez, C. (2000). *Phys* (Vol. Rev. Lett. 84).
- Chiras, D. D. (2005). *Human Biology* (5 ed.). Jones & Bartlett Learning.
- Circulation. (2008). Retrieved 2010, from Tyler Cardiovascular Consultants: <http://www.tylercvc.com/circulation.htm>
- Courtemanche, M., Ramirez, R. J., & Nattel, S. (1998). Ionic Mechanisms Underlying Human Atrial Action Potential Properties: Insights from a Mathematical Model. *Am J Physiol Heart Circ Physiol*, 275, 301-321.
- Coyne, K. S., Paramore, C., Grandy, S., Mercader, M. R., Reynolds, M., & Zimetbaum, P. (2006). Assessing the Direct Costs of Treating Nonvalvular Atrial Fibrillation in the United States. *Value in Health*, 9 (5), 348-356.
- Earley, M. J., & Schilling, R. J. (2006). Catheter and Surgical Ablation of Atrial Fibrillation. *BMJ*, 92 (2), 266-274.

- Eckstein, J., Kühne, M., Osswald, S., & Schotten, U. (2009). Applications, Mapping of Atrial Fibrillation – Basic Research and Clinical. *Swiss Med.*, 139 (35-36), 496–504.
- Elsaie, M. L., & Choudhary, S. (2010). Lasers for Scars: a Review and Evidence-Based Appraisal. *Journal of Drugs in Dermatology*, 9 (11), 1355–62.
- Enderle, J., Blanchard, S. M., & Bronzino, J. (2000). *Introduction to Biomedical Engineering*. Academic Press.
- Falk, R. H., & Podrid, P. J. (1997). *Atrial Fibrillation Mechanisms and Management* (2 ed.). Philadelphia: Lippincott-Raven.
- Feinberg WM, B. J. (1995). Prevalence, Age Distribution, and Gender of Patients with Atrial Fibrillation: Analysis and Implications. *Arch Intern Med*, 155:469-73.
- Fernández, F. A. (2006). The Atrial Fibrillation Substrate: Pulmonary Veins, Posterior Wall or Both. *Rev Esp Cardiol*, 59 (7), 643-6.
- Forbes, M. S., & Sperelakis, N. (1989). Ultra Structure of Mammalian Cardiac Muscle. In N. Sperelakis, *Physiology and Pathophysiology of the Heart* (2 ed., pp. 3-4). Boston: Kluwer Academic Publishers.
- Fowler, J. (2010). What is Atrial Fibrillation? Retrieved 02 01, 2011, from Over Lake Cardiac:
<http://overlakecardiac.blogspot.com/2010/09/what-is-atrial-fibrillation.html>
- Fuster V, R. L. (2006). ACC/AHA/ESC 2006 Guidelines for the Management of Patients with Atrial Fibrillation: a Report of the American College of Cardiology/American Heart Association Task Force on Practice Guidelines and the European Society of Cardiology Committee for Practice. *J Am Coll Cardiol.* , 149-246.
- Gerardo-Giordo, L. (2007). Modeling and Numerical Simulation of Action Potential Patterns in Human Atrial Tissues.
- Gerdes, A. M., & Kasten, F. H. (1980). Morphometric Study of Endomyocardium and Epimyocardium of the Left Ventricle in Adult Dogs. *AmJAnat*, 159, 389-394.
- Go, A. S., Hylek, E. M., Philips, K. A., Chang, Y., Henault, L. E., Selby, J. V., et al. (2001). Prevalence of Diagnosed Atrial Fibrillation in Adults. *JAMA*, 285 (18), 370-2375.

- Gregory, Y. H. (2009). Prevention of Cardiovascular Morbidity Associated With Atrial Fibrillation. Retrieved 02 28, 2010, from Medscape Education Cardiology: <http://www.medscape.org/viewarticle/708955>
- Guyton, A. C., & Hall, J. E. (1996). Textbook of Medical Physiology. Philadelphia (9 ed.). (Saunders, Ed.) W.B. Saunders Company.
- Haines, D. E. (2000). The Biophysics and Pathophysiology of Lesion Formation During Radiofrequency Catheter Ablation (3 ed.). (D. P. Zipes, & J. Jalife, Eds.) Philadelphia: W.B.Saunders Company.
- Henriquez, C. S., & Papazoglou, A. A. (1996). Using Computer Models to Understand the Roles of Tissue Structure and Membrane Dynamics in Arrhythmogenesis . Proc. IEEE, 84 (3), 334–354.
- Jacquemet, V., Oosterom, A. V., Vesin, J. M., & Kappenberger, L. (2006). Analysis of Electrocardiograms During Atrial Fibrillation. IEE Engineering in Medicine and Biology, 79-88.
- Kannel, W. B., Abbott RD, R. D., Savage, D. D., & McNamara, P. M. (1982). Epidemiological Features of Chronic Atrial Fibrillation: the Framingham Study. N Engl J Med , 306, 1018-1022.
- Katz, A. M. (2006). Physiology of the Heart (4 ed.). Philadelphia: Lippincott Williams & Wilkins.
- Khairy, P., & Nattel, S. (2002). New Insights into the Mechanisms and Management of Atrial Fibrillation. CMAJ, 167 (9), 1012-20.
- Kibble, J. D., & Halsey, C. R. (2009). Medical Physiology. McGraw Hill.
- Kijawornrat, A., Roche, B. M., & Hamlin, R. L. (2008). A Canine Model of Sustained Atrial Fibrillation Induced by Rapid Atrial Pacing and Phenylephrine. American Association for Laboratory Animal Science, 58 (5), 490–493.
- Klabunde, R. E. (2005). Cardiovascular Physiology Concepts. Philadelphia: Lippincott Williams & Wilkins.
- Klabunde, R. E. (2008). Non-Pacemaker Action Potentials. Retrieved November 29, 2010, from Cardiovascular Physiology Concepts: <http://www.cvphysiology.com/Arrhythmias/A006.htm>
- Klabunde, R. E. (2008). Sinoatrial Node Action Potentials. Retrieved November 29, 2010, from Cardiovascular Physiology Concepts: <http://www.cvphysiology.com/Arrhythmias/A004.htm>

- Lesh, D. M., Spear, F. J., & Simson, B. M. (1988). A Computer Model of the Electrogram. pp. 69-73.
- Lewis, T. (1909). Auricular Fibrillation: A Common Clinical Condition. *BMJ* , 2, 1528.
- Luo, C., & Rudy, Y. (1994). A Dynamic Model of the Cardiac Ventricular Action Potential. I. Simulations of Ionic Currents and Concentration Changes. *Circulation Research*, 74, 1071-1096.
- Malmivuo, J., & Plonsey, R. (1995). *Anatomy and Physiology of the Heart*. New York: Oxford University Press.
- Minino, A. M., Heron, M. P., Murphy, S. L., & Kochanek, K. D. (2007). Deaths: Final Data for 2004. *National Vital Statistics Reports*, 55 (19), 08-21.
- Moss, A. J., & Allen, H. D. (2007). *Moss and Adams' Heart Disease in Infants, Children, and Adolescents: Including the Fetus and Young Adult*. (H. D. Allen, D. J. Driscoll, & R. E. Shaddy, Eds.) Philadelphia, PA: Lippincott Williams & Wilkins.
- Murillo M, a. C. (2004). A Fully Implicit Parallel Algorithm for Simulating the Nonlinear Electrical Activity of the Heart. *Numerical Linear Algebra with Applications*, 261-277.
- Nithiarasu P.V, Z. O. (1998). Shock Capturing Viscosities for the General Fluid Mechanics Algorithm. *International Journal of Numerical Methods in Fluids*, 1325-1353.
- Noble, D., & Hutter, O. F. (1960). Rectifying Properties of Heart Muscle. *Nature* 188 , 495.
- Nygren, A., Fiset, C., Firek, L., Clark, J. W., Lindblad, D. S., Clark, R. B., et al. (1998). Mathematical Model of an Adult Human Atrial Cell. *Circ. Res.* 82 , 63-81.
- P. Wolf, E. B. (1996). Secular Trends in the Prevalence of Atrial Fibrillation: The Framingham Study. *Amer. Heart J*, 790-796.
- Patel, A. M., Westveer, D. C., Man, K. C., Stewart, J. R., & Frumin, H. I. (2000). Treatment of Underlying Atrial Fibrillation: Paced Rhythm Obscures Recognition. *The American College of Cardiology Foundation*, 36 (3), 784-7.
- Plonsey, R., & Roger, B. C. (2007). *Bioelectricity A Quantitative Approach* (3 ed.). Durham, NC: Springer.

- Podrid, P. J., & Kowey, P. R. (2001). *Cardiac Arrhythmia: Mechanisms, Diagnosis, and Management*. Philadelphia: Lippincott Williams & Wilkins.
- Potse, M., Dubé, B., Richer, J., Vin, A., & Gulrajani, R. M. (2006). A Comparison of Monodomain and Bidomain Reaction-Diffusion Models for Action Potential Propagation in the Human Heart. *IEEE Transactions on Biomedical Engineering*, 53 (12).
- Rosenthal, L. (2010). Atrial Fibrillation. Retrieved September 20, 2010, from Emedicine: <http://emedicine.medscape.com/article/151066-overview>
- Rosolen A, O. S. (2006). "Numerical Schemes for the Simulation of Three-Dimensional Cardiac Electrical Propagation in Patient-Specific Ventricular Geometries". Egmond and Zee, The Netherlands, 5-8.
- Roth, B. J. (1991). Action Potential Propagation in a Thick Strand of Cardiac Muscle. *Circ. Res.* , 68, 162-173.
- Schaper, J., Meiser, E., & Stammler, G. (1985). Ultra Structural Morphometric Analysis of Myocardium from Dogs, Rats, Hamsters, Mice, and from Human Hearts. *Circulation Research*, 56, 377-391.
- Schoenstadt, A. (2006). Paroxysmal Atrial Fibrillation. Retrieved September 20, 2010, from MedTV: <http://heart.emedtv.com/paroxysmal-atrial-fibrillation/paroxysmal-atrial-fibrillation.html>
- Severs, N. J., Slade, A. M., Powell, T., Twist, V. W., & Jones, G. E. (1985). Morphometric Analysis of the Isolated Calcium Tolerant Cardiacmyocyte. *CellTissueRes*, 240, 159-168.
- Skouibine, K., Trayanova, N., & Moore, P. (2000). A Numerically Efficient Model for Simulation of Defibrillation in an Active Bidomain Sheet of Myocardium. *Math. Biosci*, 166, 85-100.
- Song, H. K., & Puskas, J. D. (2004). Recent Advances in Surgery for Atrial Fibrillation. Retrieved November 10, 2010, from CTSNet: <http://www.ctsnet.org/sections/newsandviews/specialreports/article-1.html>
- Starr, C., & McMillan, B. (2007). *Human Biology* (8 ed.). (P. Williams, Ed.) Belmont, CA: Yolando Cossio.
- Stewart, S., Hart, C., & Hole, D. J. (2002). A Population-Based Study of the Long- Term Risks Associated with Atrial Fibrillation: 20-Year Follow-Up of the Renfrew/Paisley Study. *Am J Med*, 113 (5), 359-364.

- Thomas, S. P. (1999). Intraoperative Endocardial Radiofrequency Ablation for Atrial Fibrillation. Argentine Federation of Cardiology .
- Wu, E. Q., Birnbaum, H. G., Mareva, M., Tuttle, E., Castor, A. R., Jackman, W., et al. (2005). Economic Burden and Co-Morbidities of Atrial Fibrillation in a Privately Insured Population. Current Medical Research and Opinion, 21 (10), 1693-1699.
- X.C., M. M. (2004). A Fully Implicit Parallel Algorithm for Simulating the Nonlinear Electrical Activity of the Heart. Numerical Linear Algebra with Applications, 261-277.
- Yanowitz, F. G. (n.d.). The Standard 12 Lead ECG. Retrieved November 29, 2010, from ECG Learning Center:
http://library.med.utah.edu/kw/ecg/ecg_outline/Lesson1/index.html#orientation

APPENDICES

Appendix I Glossary
(Courtemanche et al. 1998)

[Ca] _{Cmdn}	Ca ²⁺ bound calmodulin concentration	f _{NaK}	Voltage-dependence parameter for I _{NaK}
[Ca] _{Csqn}	Ca ²⁺ bound calsequestrin concentration	g _{b,Ca}	Maximal I _{b,Ca} conductance
[Ca] _{rel}	Ca ²⁺ concentration in release compartment	g _{b,Na}	Maximal I _{b,Na} conductance
[Ca] _{Trpn}	Ca ²⁺ bound troponin concentration	g _{Ca,L}	Maximal I _{Ca, L} conductance
[Ca] _{up}	Ca ²⁺ concentration in uptake compartment	g _{K1}	Maximal I _{K1} conductance
[Ca] _{up(max)}	Maximal Ca ²⁺ concentration in NSR	g _{Kr}	Maximal I _{Kr} conductance
[Cmdn] _{max}	Total calmodulin concentration in myoplasm	g _{Ks}	Maximal I _{Ks} conductance
[Trpn] _{max}	Total troponin concentration in myoplasm	g _{Kur}	Maximal I _{Kur} conductance
[X] _i	Intracellular concentration of ion X	g _{Na}	Maximal I _{Na} conductance
[X] _o	Extracellular concentration of ion X	g _{to}	Maximal I _{to} conductance
AP	Human atrial action potential	h	Fast inactivation gating variable for I _{Na}
C _m	Membrane capacitance	I _{b,Ca}	Background Ca ²⁺ current
Cmdn	Calmodulin, sarcoplasmic Ca ²⁺ buffer	I _{b,Na}	Background Na ⁺ current
Csqn	Calsequestrin, JSR Ca ²⁺ buffer	I _{Ca,L}	L-type inward Ca ²⁺ current
d	Activation gating variable for I _{Ca,L}	I _{ion}	Total ionic current
D _e	Extracellular conductivity tensor	I _{K1}	Inward rectifier K ⁺ current
D _i	Intracellular conductivity tensor	I _{kr}	Rapid delayed ractifier K ⁺ current
Ex	Equilibrium potential for ion x	I _{ks}	Slow delayed ractifier K ⁺ current
F	Faraday constant	I _{kur}	Ultrarapid delayed ractifier K ⁺ current
f	Voltage dependent inactivation gating variable for I _{Ca,L}	I _m	membrane current
fCa	Ca ²⁺ -dependent inactivation gating variable for I _{Ca, L}	I _{Na}	Fast inward Na ⁺ current
F _n	Sarcoplasmic Ca flux signal for I _{rel}	I _{NaCa}	Na ⁺ / Ca ²⁺ exchanger current

Appendix I (Continued)

$I_{NaCa(max)}$	I_{NaCa} scaling factor	R	Gas constant
I_{NaK}	$Na^+ - K^+$ pump current	SR	Sarcoplasmic reticulum
$I_{NaK(max)}$	Maximal I_{NaK}	S_v	Ratio of membrane surface area to tissue volume
$I_{p,Ca}$	Sarcoplasmic Ca^{2+} pump current	T	Temperature
$I_{p,Ca(max)}$	Maximal $I_{p,Ca}$	Trpn	Troponin, sarcoplasmic Ca^{2+} buffer
I_{rel}	Ca^{2+} release current from the JSR	u	Activation gating variable for I_{rel}
I_{st}	Stimulus current	u_a	Activation gating variable for I_{kur}
I_{to}	Transient outward K^+ current	u_i	Inactivation gating variable for I_{kur}
I_{tr}	Ca^{2+} transfer current from NSR to JSR	V	Transmembrane Potential
I_{up}	Ca^{2+} uptake current into the NSR	(z) v	Ca^{2+} flux-dependent inactivation gating variable for I_{rel}
$I_{up(max)}$	Maximal Ca^{2+} uptake rate for I_{up}	V_{Cell}	Volume cell
$I_{up,leak}$	Ca leak current from the NSR	V_i	Intracellular volume
j	Slow inactivation gating variable for I_{Na}	V_{rel}	SR release compartment volume
JSR	Junctional SR, SR release compartment	V_{up}	SR uptake compartment volume
K_{Q10}	Q_{10} -based temperature adjustment factor	w	Voltage-dependent Inactivation gating variable for I_{rel}
k_{rel}	Maximal Ca^{2+} release rate for I_{rel}	$x_{\infty} (x_{ss})$	Steady-state relation for gating variable x
m	Activation gating variable for I_{Na}	x_r	Activation gating variable for I_{kr}
NSR	Network SR, SR uptake compartment	x_s	Activation gating variable for I_{ks}
o_a	Activation gating variable for I_{to}	α_x	Forward rate constant for gating variable x
o_i	Inactivation gating variable for I_{to}	β_x	Backward rate constant for gating variable x
Q_{10}	Temperature adjustment factor	γ	Voltage-dependence parameter for I_{NaCa}

Appendix I (Continued)

σ	[Na ⁺] _o dependence parameter for I _{NaK}
τ_{tr}	Ca ²⁺ transfer time constant
τ_x	Time constant for gating variable x
ϕ_e	Extracellular potential
ϕ_i	Intracellular potential

Appendix II Model Constants

(Courtemanche et al. 1998)

Constants	Definition	Value	Unit
R	Gas constant	8.31	J.K ⁻¹ .mol ⁻¹
T	Temperature	310	K
F	Faraday constant	96.49	C/mmol
C _m	Membrane capacitance	1	μF/cm ²
V _i	Intracellular volume	13668	μm ³
V _{up}	SR uptake compartment volume	1109.52	μm ³
V _{rel}	SR release compartment volume	96.48	μm ³
[K ⁺] _o	Extracellular concentration of K ⁺	5.4	mM
[Na ⁺] _o	Extracellular concentration of Na ⁺	140	mM
[Ca ²⁺] _o	Extracellular concentration of Ca ²⁺	1.8	mM
g _{Na}	Maximal I _{Na} conductance	7.8	nS/pF
g _{k1}	Maximal I _{K1} conductance	0.09	nS/pF
g _{to}	Maximal I _{to} conductance	0.1652	nS/pF
g _{Kr}	Maximal I _{Kr} conductance	0.0294	nS/pF
g _{Ks}	Maximal I _{Ks} conductance	0.129	nS/pF
g _{Ca,L}	Maximal I _{Ca,L} conductance	0.1238	nS/pF
g _{b,Ca}	Maximal I _{b,Ca} conductance	0.00113	nS/pF
g _{b,Na}	Maximal I _{b,Na} conductance	0.000674	nS/pF
I _{NaK(max)}	Maximal I _{NaK}	0.6	pA/pF
I _{NaCa(max)}	Maximal I _{NaCa}	1600	pA/pF
I _{p,Ca(max)}	Maximal I _{p,Ca}	0.275	pA/pF
I _{up(max)}	Maximal I _{up}	0.005	mM/ms
K _{Q10}	Temperature adjustment factor for I _{kur} and I _{to} kinetics	3	
γ	Voltage-dependence parameter for I _{NaCa}	0.35	
K _{m,Na(i)}	[Na ⁺] _i half-saturation constant for I _{NaK}	10	mM
K _{m,Na(o)}	[Na ⁺] _o half-saturation constant for I _{NaK}	1.5	mM
K _{m,Na}	[Na ⁺] _o saturation constant for I _{NaCa}	87.5	mM
K _{m,Ca}	[Ca ²⁺] _o half-saturation constant for I _{NaCa}	1.38	
K _{sat}	Saturation factor for I _{NaCa}	0.1	
k _{rel}	Maximal Ca ²⁺ release rate for I _{rel}	30	ms ⁻¹
k _{up}	[Ca ²⁺] _o half-saturation constant for I _{up}	0.00092	mM
[Ca] _{up(max)}	Maximal Ca ²⁺ concentration in uptake compart.	15	mM

Appendix II (Continued)

Constants	Definition	Value	Unit
$[\text{Cmdn}]_{\text{max}}$	Total calmodulin concentration in myoplasm	0.05	mM
$[\text{Trpn}]_{\text{max}}$	Total troponin concentration in myoplasm	0.07	mM
$[\text{Csqn}]_{\text{max}}$	Total Calsequestrin concentration in myoplasm	10	mM
$K_{\text{m,Cmdn}}$	$[\text{Ca}^{2+}]_i$ half-saturation constant for calmodulin	0.00238	mM
$K_{\text{m,Trpn}}$	$[\text{Ca}^{2+}]_i$ half-saturation constant for troponin	0.0005	mM
$K_{\text{m,Csqn}}$	$[\text{Ca}^{2+}]_{\text{rel}}$ half-saturation constant for I_{up}	0.8	mM
S_v	Ratio of membrane surface area to tissue volume	0.024	cm ⁻¹
D_e	Extracellular conductivity tensor	1.68	mS/cm
D_i	Intracellular conductivity tensor in x direction	5.6	mS/cm

Appendix III Copyright Permissions

III.1 Copyright Permission Request FIGURES 3 - 1 and 3 - 2

Richard Klabunde <reklabunde@gmail.com>

Wed, Jun 8, 2011 at 8:38
AM

To: Samineh Esfahani <sesfahan@mail.usf.edu>

Samineh,

You have my permission to use the following two figures in your thesis:

<http://www.cvphysiology.com/Arrhythmias/A006.htm>

<http://www.cvphysiology.com/Arrhythmias/A004.htm>

This permission extends to any future revisions, editions, and translations provided that my name and website are cited as the source for these figures.

Sincerely,

Richard Klabunde, Ph.D.
Ohio University
Athens, Ohio
[Quoted text hidden]

Appendix III (Continued)

III.2 Copyright Permission Request FIGURE 2 - 2

Samineh Esfahani <sesfahan@mail.usf.edu>

Tue, Jun 7, 2011 at 9:07
PM

To: ewu@analysisgroup.com

Dear Mr. Wu:

I am a student at the University of South Florida and am completing master thesis titled “**Two-Dimensional Computer Model of Human Atrial Ablation.**” I would like your permission to reprint in my work excerpts from the work identified below: Chapter 2 Wu, E. Q., Birnbaum, H. G., Mareva, M., Tuttle, E., Castor, A. R., Jackman, W., et al. (2005). Economic burden and co-morbidities of atrial fibrillation in a privately insured population. *Current Medical Research and Opinion* , 21 (10), 1693-1699.

The excerpts of the work to be reproduced in my work are attached in this Email.

I am requesting permission to include these excerpts in my work and plan to distribute the work freely via the internet. I am requesting that your permission extends to any future revisions, editions, and translations of this work made by me or on my behalf . If you approve of the use requested above, kindly respond to my Email. My thesis submission deadline is June 25th, 2011.

I sincerely appreciate it. If you have any questions or concerns, please do not hesitate to contact me, either by phone at [813-420-5353](tel:813-420-5353) or by email at sesfahan@mail.usf.edu

Samineh R. Esfahani
College of Engineering
University of South Florida
4202 E. Fowler Ave, ENB 118
Tampa, FL 33620

Wu, Eric <EWu@analysisgroup.com>

Thu, Jun 9, 2011 at 7:37 AM

To: Samineh Esfahani <sesfahan@mail.usf.edu>

Yes, it is approved. best, Eric

Appendix III (Continued)

III.3 Copyright Permission Request

Samineh Esfahani <sesfahan@mail.usf.edu>

Tue, Jun 14, 2011 at 7:32 PM

To: mail@medmovie.com

Dear Permissions Coordinator:

I am a student at the University of South Florida and am completing master thesis titled “**Two-Dimensional Computer Model of Human Atrial Ablation.**” I would like your permission to use a video animation called: Atrial Fib. Ablation with the following web address:

<http://www.medmovie.com/mmdatabase/MediaPlayer.aspx?ClientID=13&TopicID=837>

I am requesting permission to include this excerpt in my thesis presentation only. If you approve of the use requested above, kindly respond to my Email. My thesis submission deadline is June 25th, 2011.

I sincerely appreciate it. If you have any questions or concerns, please do not hesitate to contact me, either by phone at [813-420-5353](tel:813-420-5353) or by email at sesfahan@mail.usf.edu

Samineh R. Esfahani
College of Engineering
University of South Florida
4202 E. Fowler Ave, ENB 118
Tampa, FL 33620

Rick Gersony <rgersony@gmail.com>

Tue, Jun 14, 2011 at 10:04 PM

To: Samineh Esfahani <sesfahan@mail.usf.edu>

Yes you have permission.

Best Regards,

Rick Gersony

CEO

Medmovie

Appendix III (Continued)

III.4 Copyright Permission Request FIGURE 3 - 3

Jones, Jennifer (ELS-OXF) <J.Jones@elsevier.com> **Wed, Jun 22, 2011 at 11:28 AM**
To: Samineh Esfahani <sesfahan@mail.usf.edu>

Dear Samineh R. Esfahani

We hereby grant you permission to reproduce the material detailed below at no charge **in your thesis, in print and on the University of South Florida web sites** subject to the following conditions:

1. If any part of the material to be used (for example, figures) has appeared in our publication with credit or acknowledgement to another source, permission must also be sought from that source. If such permission is not obtained then that material may not be included in your publication/copies.
2. Suitable acknowledgment to the source must be made, either as a footnote or in a reference list at the end of your publication, as follows:
"This article was published in Publication title, Vol number, Author(s), Title of article, Page Nos, Copyright Elsevier (or appropriate Society name) (Year)."
3. Your thesis may be submitted to your institution in either print or electronic form.
4. Reproduction of this material is confined to the purpose for which permission is hereby given.
5. This permission is granted for non-exclusive world **English** rights only. For other languages please reapply separately for each one required. Permission excludes use in an electronic form other than as specified above. Should you have a specific electronic project in mind please reapply for permission.
6. This includes permission for UMI to supply single copies, on demand, of the complete thesis. Should your thesis be published commercially, please reapply for permission.

Yours sincerely
Jennifer Jones
Rights Associate

Appendix III (Continued)

III.5 Courtemanche et al. FIGURES

Request for Permission to Reproduce Previously Published Material

(please save this file to your desktop, fill out, **save again**, and e-mail to permissions@the-aps.org)

Your Name: Samineh R. Esfahani E-mail: sesfahan@mail.usf.edu

Affiliation: University of South Florida

University Address (for PhD students): 4202 E. Fowler Ave, ENB 118 Tampa, FL 33620

Description of APS material to be reproduced (check all that apply):

- Figure Partial Article Abstract
 Table Full Article Book Chapter
Other (please describe):

Please provide all applicable information about the APS material you wish to use:

Author(s): Courtemanche, M., Ramirez, R. J., & Nattel, S.
Article or Chapter Title: Ionic mechanisms underlying human atrial action potential properties: insights from
Journal or Book Title: Am J Physiol Heart Circ Physiol
Volume: 275 Page No(s): 301-321 Figure No(s): All 20 Table No(s): All 3
Year: 1998 DOI: _____

(If you are reproducing figures or tables from more than one article, please fill out and send a separate form for each citation.)

Please provide all applicable information about where the APS material will be used:

How will the APS material be used? (please select from drop-down list) Dissertation
If "other," please describe:

Title of publication or meeting where APS material will be used (if used in an article or book chapter, please provide the journal name or book title as well as the article/chapter title):

Two-Dimensional Computer Model of Human Atrial Ablation

Publisher (if journal or book): N/A

URL (if website): Not Known Yet

Date of Meeting or Publication: July 5, 2011

Will readers be charged for the material: Yes No

Additional Information:

APPROVED
By pripka at 11:28 am, Jun 08, 2011

THE AMERICAN PHYSIOLOGICAL SOCIETY
9650 Rockville Pike, Bethesda, MD 20814-3991

Permission is granted for use of the material specified above, provided the publication is credited as the source, including the words "used with permission."



Publications Manager & Executive Editor